mathematics

MDPI

Article

Multi-Objective Identification and Optimal Control for Generalized SIR Epidemic Models with Time-Dependent Parameters

Aníbal Coronel [1,*], Ana Paula Chorobura [2], Camila Isoton [3] and Fernando Huancas [4,*]

[1] Departamento de Ciencias Básicas–Centro de Ciencias Exactas, Facultad de Ciencias, Universidad del Bío-Bío, Campus Fernando May, Chillán 3780000, Chile
[2] Instituto de Matemática, Universidade Federal de Mato Grosso do Sul, Campo Grande 79074-460, Brazil; ana.chorobura@ufms.br
[3] Faculdade de Ciências Exatas e Tecnologia, Universidade Federal da Grande Dourados, Dourados 79804-970, Brazil; camilaisoton@ufgd.edu.br
[4] Departamento de Matemática, Facultad de Ciencias Naturales, Matemáticas y del Medio Ambiente, Universidad Tecnológica Metropolitana, Las Palmeras No. 3360, Ñuñoa, Santiago 7800003, Chile
* Correspondence: acoronel@ubiobio.cl (A.C.); fhuancas@utem.cl (F.H.)

Abstract

This paper investigates a multi-objective optimization framework for the simultaneous parameter identification and optimal vaccination control of a generalized non-linear SIR epidemic model. In contrast to traditional single-objective approaches, we formulate a vector optimization problem to concurrently minimize deviations from observed trajectories, disease prevalence, and public health operational costs, unlocking the identification of Pareto-optimal strategies. We establish the global existence, uniqueness, and physical invariance of the state solutions within a classical Sobolev space framework by employing a contraction mapping argument under the Bielecki weighted norm. Via the direct method of the calculus of variations and compact Sobolev embeddings, the existence of weak Pareto-optimal solutions is rigorously proved. First-order necessary optimality conditions are subsequently derived using the geometric Dubovitskii–Milyutin functional formalism, which yields a well-posed backward linear adjoint system and a precise characterization of the coupled variational inequalities. Finally, we implement a robust numerical architecture driven by an adjoint-based Augmented Lagrangian Method coupled with a quasi-Newton solver over a piecewise linear continuous subspace for the approximation and simulation of the Pareto-optimal frontier, which is successfully validated through three distinct numerical examples.

Keywords: parameter identification; control problem; inverse problem; SIR model

MSC: 93B30; 92D30; 49K15; 34H05

Check for updates

Academic Editor: Jonathan Blackledge

Received: 1 October 2026
Revised: 23 October 2026
Accepted: 24 October 2026
Published: 28 October 2026

Copyright: © 2026 by the authors. Licensee MDPI, Basel, Switzerland. This article is an open access article distributed under the terms and conditions of the Creative Commons Attribution (CC BY) license.

1. Introduction

The mathematical modeling of infectious diseases by the application of deterministic differential equations has become an essential framework for understanding, predicting, and mitigating transmission dynamics [1,2]; for further details, see the recent survey [3]. Since the seminal formulations of compartmental structures introduced by Kermack and McKendrick [4], the integration of intervention strategies within these systems has evolved significantly [5,6]. In particular, at the beginning of the 21st century, Behncke [7] established

a rigorous mathematical foundation for the optimal control of deterministic epidemics, demonstrating how dynamic public health measures such as vaccination or treatment can effectively minimize both disease prevalence and implementation costs. Over the years, these control frameworks have been extended to accommodate more sophisticated biological behaviors, including spatial diffusion and non-linear forces of infection. Recently, Coronel et al. [8] expanded this analysis by simultaneously addressing optimal control problems and parameter identification in reaction–diffusion systems with generalized transmission forces. Building upon these classical and recent insights into epidemic management, this paper investigates the optimal control of the generalized model inspired by Behncke [7]. However, rather than limiting the analysis to a single-objective framework, and following the multi-objective perspectives discussed by Fernández-Cara [9] we employ a multi-objective optimization approach to simultaneously regulate the implementation of the vaccination campaign and minimize the total number of infected individuals. This framework allows for a rigorous identification of Pareto-optimal strategies that balance public health interventions against operational costs.

Let us introduce a summary of the model considered by Behncke [7] and the model considered in the present work. We begin by recalling that the fundamental assumptions of the compartmental methodology assume that a total population consisting of N individuals is divided into three distinct classes: susceptible (s), infected (i), and recovered (r), such that the dynamics of the disease are governed by the following system of ordinary differential equations:

$$s'(t) = -\beta si, \quad i'(t) = \beta si - \gamma i, \quad \text{and} \quad r'(t) = \gamma i,$$

where β and γ denote the transmission and recovery rates, respectively. To extend this classical framework, Behncke [7] introduced three major refinements to the compartmental dynamics (see Figure 1). First, to capture more realistic epidemiological transmission features, the traditional bilinear incidence rate SI or mass action law is generalized by considering a non-linear infection force $f(S, I)$ satisfying:

$$\left.\begin{array}{l} f : [0,N]^2 \to [0,\infty);\ f \in C^2((0,N)^2, \mathbb{R}); \\ f(0,i) = f(s,0) = 0,\ f > 0,\ \text{on } (0,N]^2; \\ f_s > 0, \quad f_i > 0, \quad f_{si} > 0, \\ \qquad f_{ss} \le 0, \quad f_{ii} \le 0, \quad \text{on } [0,N]^2. \end{array}\right\} \tag{1}$$

Second, a parameter $p \in [0,1]$ is introduced to split the transmission path, assuming that a fraction $1-p$ of newly exposed individuals bypasses the active infectious state I due to robust innate immunity or immediate subclinical clearance, thereby transitioning directly into the recovered class. Third, the term $u(t)g(s)$, where $u(t)$ acts as a control variable and $g(s)$ denotes a generic nonlinear function representing a state-dependent removal rate, is incorporated to model generic external mitigation mechanisms, such as the deployment of reactive prophylaxis, isolation protocols, or emergency vaccination campaigns, fulfilling the regularity assumptions:

$$\left.\begin{array}{l} g : [0,N] \to [0,\infty),\ g \in C^1((0,N), \mathbb{R}), \\ g(0) = 0,\ g'(s) \ge 0;\ g'(0) > 0. \end{array}\right\} \tag{2}$$

Furthermore, in this paper we consider that β and γ are time-dependent functions. Specifically, the mathematical model considered in this paper is given by

$$s'(t) = -\beta(t) f(s,i) - u(t) g(s), \tag{3}$$

$$i'(t) = p\beta(t) f(s,i) - \gamma(t) i, \tag{4}$$

$$r'(t) = u(t) g(s) + (1-p)\beta(t) f(s,i) + \gamma(t) i, \tag{5}$$

$$(s(0), i(0), r(0)) = (s_0, i_0, r_0), \tag{6}$$

where $(s_0, i_0, r_0) \in [0, N]^3$ are the initial conditions.

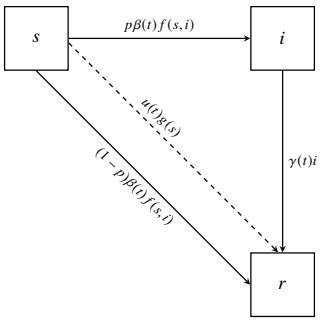

Figure 1. Compartmental diagram for the generalized epidemic system considered in this paper (see (3)–(6)), where solid arrows represent natural epidemiological transitions and the dashed arrow denotes the external, state-dependent mitigation control pathway.

The main aim of this paper is three-fold: first, to identify the transmission and recovery rates from experimental measurements of the susceptible, infected, and recovered populations; second, to determine the optimal control variable $u(t)$ that minimizes the total vaccination effort; and third, to minimize the total number of infected individuals. We define the cost functionals $J_i = J_i(s, i, r, u)$ corresponding to each of these cases and the objective vector functional by the following relations

$$J_1 = \frac{1}{2} \int_0^T \|(s, i, r)(t) - (s^{\text{obs}}, i^{\text{obs}}, r^{\text{obs}})(t)\|^2 \, dt, \tag{7}$$

$$J_2 = \int_0^T i(t) \, dt, \quad J_3 = \int_0^T u(t) \, dt. \tag{8}$$

$$\mathbf{J} = (J_1, J_2, J_3)^T \tag{9}$$

Moreover, we consider the admissible set

$$\begin{aligned} \mathcal{U}_{\text{ad}} = \Big\{ & (\beta, \gamma, u) \in L^\infty(0, T)^3 \ \mid \\ & 0 < \beta_{\min} \le \beta(t) \le \beta_{\max}, \ 0 < \gamma_{\min} \le \gamma(t) \le \gamma_{\max}, \\ & 0 \le u(t) \le u_{\max} \text{ a.e. } t \in [0, T] \Big\}. \end{aligned} \tag{10}$$

Then, the multi-objective optimization problem for parameter identification and vaccination control is defined as follows:

$$\min_{(\beta, \gamma, u) \in \mathcal{U}_{\text{ad}}} \mathcal{J}(\beta, \gamma, u), \tag{11}$$

$$\text{subject to the non-linear state Equations (3)–(6).} \tag{12}$$

Henceforth, $\mathcal{J}(\beta, \gamma, u) = \mathbf{J}(S_{\beta,\gamma,u}, I_{\beta,\gamma,u}, R_{\beta,\gamma,u}, u)$ is the reduced cost function. The notation $(S_{\beta,\gamma,u}, I_{\beta,\gamma,u}, R_{\beta,\gamma,u})$ is introduced to emphasize that the solution to the state system (3)–(6) depends implicitly on the parameter–control tuple (β, γ, u).

In this context, it should be highlighted that there is a competing nature among the objective functions; for instance, a reduction in disease prevalence J_2 typically demands an escalation in the vaccination effort J_3. Consequently, a single global optimum that minimizes all criteria simultaneously does not exist. Therefore, in the present work, the multi-objective optimization problem (11) and (12) is analyzed through the concept of Pareto optimality [10–12]. Briefly, an admissible decision vector $(\beta^*, \gamma^*, u^*) \in \mathcal{U}_{\text{ad}}$ is said to be weak Pareto optimal if there is no other feasible vector $(\beta, \gamma, u) \in \mathcal{U}_{\text{ad}}$ such that $\mathcal{J}_k(\beta, \gamma, u) \le \mathcal{J}_k(\beta^*, \gamma^*, u^*)$ for all $k \in \{1, 2, 3\}$. The collection of all such non-dominated points defines the Pareto front, providing a rigorous mathematical foundation for public

health decision-makers to evaluate trade-offs between epidemiological control and economic constraints.

Hereinafter by notational convenience we introduce a vectorial notation for state and parameter–control variables. More precisely we consider that

$$\mathbf{x}(t) = \Big(s(t), i(t), r(t)\Big)^{\top}, \tag{13}$$

$$\mathbf{v}(t) = \Big(\beta(t), \gamma(t), u(t)\Big)^{\top}, \tag{14}$$

$$\begin{aligned}\mathbf{F}(t, \mathbf{x}; \mathbf{v}) = \Big(& -v_1(t) f(x_1, x_2) - v_3(t) g(x_1), \\ & p v_1(t) f(x_1, x_2) - v_2(t) x_2, \\ & v_3(t) g(x_1) + (1-p) v_1(t) f(x_1, x_2) + v_2(t) x_2 \Big)^{\top},\end{aligned} \tag{15}$$

$$\mathbf{x}_0 = \Big(s_0, i_0, r_0\Big)^{\top}, \tag{16}$$

$$\text{State system (3)–(6): } \mathbf{x}'(t) = \mathbf{F}(t, \mathbf{x}; \mathbf{v}),\ \mathbf{x}(0) = \mathbf{x}_0. \tag{17}$$

Here, the superscript $\top$ denotes the transpose of the vector.

The main five contributions of this work are summarized as follows. First, we establish the global existence, uniqueness, and boundedness of the state system solution within the Sobolev space $W^{1,2}([0,T];\mathbb{R}^3)$ by applying a contraction mapping argument coupled with the Bielecki weighted norm. Second, we prove the existence of at least one weak Pareto-optimal solution for the simultaneous parameter identification and vaccination control problem via the direct method of the calculus of variations, tracking minimizing sequences under sequential weak compactness and compact Sobolev embeddings. Third, we define a mathematically consistent backward linear adjoint system, rigorously demonstrating its well-posedness in $W^{1,2}([0,T];\mathbb{R}^3)$ by using time-reversal transformations and Carathéodory weak solution formulations. Fourth, we derive the complete first-order necessary optimality conditions and characterize the variational inequalities for the time-dependent parameters and control functions by applying the Dubovitskii–Milyutin formalism [13–16]. Finally, we develop a numerical approximation of the multi-objective optimization problem and present some numerical examples.

In the literature, the simultaneous study of parameter identification and optimal control for epidemiological models has been predominantly addressed through single-objective optimization frameworks, as exemplified and reviewed in the recent work of Coronel et al. [8]. For multi-objective formulations in epidemiological systems, some related works can be highlighted (see, e.g., Refs. [17–20]), although this list is by no means exhaustive. It is essential to emphasize that the results of those previous studies differ significantly from the insights obtained in the present paper. First, many existing frameworks focus primarily on experimental data fitting and practical applications, whereas this work introduces a mathematically rigorous, self-contained functional framework based on Sobolev spaces. Second, the underlying state dynamics in the literature often cover more restrictive compartmental structures, or assume specific, simplified forms of the incidence force $f(S,I)$ and the vaccination response $g(S)$, which can be regarded as particular cases of the general Behncke-type non-linear functions analyzed herein. Finally, from a computational perspective, the numerical methodology proposed in this paper differs from prior approaches that frequently rely on "black-box" optimization routines without explicitly detailing the underlying continuous-to-discrete spaces projection. Conversely, our scheme provides a transparent and verifiable discretization.

The remainder of this paper is organized as follows. Section 2 develops the rigorous analysis of the state equations, establishing the solution properties in the Sobolev framework. In Section 3, we present the proof of the existence of weak Pareto-optimal

solutions for the multi-objective optimization problem. Section 4 is dedicated to introducing the notation and results which are relevant to apply the Dubovitskii–Milyutin formalism. Section 5 is devoted to the derivation of the first-order necessary optimality conditions via the Dubovitskii–Milyutin formalism. Section 6 outlines the finite-dimensional discretization scheme, the algorithmic implementation, and provides the numerical simulations alongside the approximation of the Pareto frontier. Finally, Section 7 delivers the concluding remarks and future research directions.

2. Well-Posedness of the State Equations

In this section, we develop the analysis of the existence, uniqueness, and regularity of solutions for the mathematical model (3)–(6) within the framework of Sobolev spaces; see [21,22] for details. We remark that the selection of the Sobolev functional framework for the state variables, rather than the standard space of continuously differentiable functions, is a direct consequence of the L^∞ regularity prescribed in the admissible set $\mathcal{U}_{\text{ad}}$. This setting provides a more natural context for analyzing optimal control problems, since functions belonging to $\mathcal{U}_{\text{ad}}$ are allowed to possess jump discontinuities (representing abrupt policy changes or reactive emergency campaigns). As a result, the derivatives of the state variables inherit these discontinuities, implying that the states cannot be classically differentiable. Here, we remark that $\mathcal{U}_{\text{ad}} \subset L^\infty(0,T)^3 \subset L^2(0,T)^3$, then the differential equations are naturally understood in the sense of Carathéodory. Furthermore, from an optimization perspective, this Sobolev space framework is essential to guarantee the weak compactness properties required for the existence of optimal controls, to rigorously derive the adjoint equations, and to ensure the convergence of the gradient-based numerical algorithms utilized to compute the Pareto-optimal frontier.

Theorem 1. *Consider the notation (14)–(17) with f and g satisfying the assumptions (1) and (2), respectively. For any $\mathbf{v} \in \mathcal{U}_{ad}$ and $\mathbf{x}_0 \in [0,N]^3$, there exists a unique solution to the initial value problem (3)–(6) such that $\mathbf{x} \in W^{1,2}([0,T];\mathbb{R}^3)$. Furthermore, the system of differential equations is satisfied for almost every (a.e.) $t \in [0,T]$ with respect to the Lebesgue measure, and the solution remains invariant within the biologically relevant region, i.e., $\mathbf{x}(t) \in [0,N]^3$ for all $t \in [0,T]$.*

Proof. The proof is based on the application of fixed–point arguments and is developed in a modified two-step regularity argument. First, since the Behncke-type non-linear functionalities f and g are continuously differentiable on the compact domain $[0,N]^3$, they are locally Lipschitz continuous and can be extended to globally Lipschitz continuous functions on $\mathbb{R}^3$. We establish the global existence and uniqueness of a continuous solution via the Banach Fixed-Point Theorem on the entire space $C([0,T];\mathbb{R}^3)$ endowed with the Bielecki weighted norm. Subsequently, we prove the physical invariance within $[0,N]^3$ a posteriori, and finally, we utilize the continuity and boundedness of this solution to prove that its weak derivative belongs to $L^2([0,T];\mathbb{R}^3)$, deducing the desired $W^{1,2}([0,T];\mathbb{R}^3)$ regularity.

We begin by noticing that the non-linear system (3)–(6) is equivalent to the integral equation

$$\mathbf{x}(t) = \mathbf{x}_0 + \int_0^t \mathbf{F}(s,\mathbf{x}(s))\,ds, \quad t \geq 0. \tag{18}$$

To analyze (18) in $C([0,T];\mathbb{R}^3)$, we consider the Bielecki weighted norm on the whole space:

$$\|\mathbf{x}\|_\lambda = \max_{t\in[0,T]} e^{-\lambda t}\|\mathbf{x}(t)\|_1, \quad \|\mathbf{x}\|_1 = |x_1| + |x_2| + |x_3|, \tag{19}$$

for $\lambda > 0$, and define the operator $\mathcal{T} : C([0,T];\mathbb{R}^3) \to C([0,T];\mathbb{R}^3)$ by the following relation

$$(\mathcal{T}\mathbf{x})(t) = \mathbf{x}_0 + \int_0^t \mathbf{F}(s,\mathbf{x}(s);\mathbf{v}(s))\,ds. \tag{20}$$

We note that $C([0,T];\mathbb{R}^3)$ is a Banach space when endowed with the norm $\|\mathbf{x}\|_\lambda$. By leveraging the globally Lipschitz extended vector field $\mathbf{F}$, the proof of existence and uniqueness of solutions for (18) reduces to verifying the hypotheses of the Banach Fixed-Point Theorem on the whole space.

$\mathcal{T}$ *is a strict Contraction mapping.* To prove that $\mathcal{T}$ is a strict contraction we select $\mathbf{x},\mathbf{y} \in C([0,T];\mathbb{R}^3)$. By virtue of the globally Lipschitz continuous extension of the field, the non-linearities f and g satisfy the Lipschitz condition on $\mathbb{R}^3$ with Lipschitz constants L_f and L_g, respectively. For almost every $s \in [0,T]$, we estimate the difference $\|\mathbf{F}(s,\mathbf{x}(s);\mathbf{v}(s)) - \mathbf{F}(s,\mathbf{y}(s);\mathbf{v}(s))\|_1$ by gathering the coefficients:

$$\begin{aligned}
&|F_1(s,\mathbf{x};\mathbf{v}) - F_1(s,\mathbf{y};\mathbf{v})| \\
&\quad \le \beta_{\max} L_f(|x_1 - y_1| + |x_2 - y_2|) + u_{\max} L_g |x_1 - y_1|, \\
&|F_2(s,\mathbf{x};\mathbf{v}) - F_2(s,\mathbf{y};\mathbf{v})| \\
&\qquad \le \beta_{\max} L_f(|x_1 - y_1| + |x_2 - y_2|) + \gamma_{\max} |x_2 - y_2|, \\
&|F_3(s,\mathbf{x};\mathbf{v}) - F_3(s,\mathbf{y};\mathbf{v})| \\
&\qquad \le u_{\max} L_g |x_1 - y_1| + \beta_{\max} L_f(|x_1 - y_1| + |x_2 - y_2|) \\
&\qquad\quad + \gamma_{\max} |x_2 - y_2|.
\end{aligned}$$

Summing these bounds reveals that there exists a positive constant $L_0 > 0$ depending only on the bounds of $\mathcal{U}_{\text{ad}}$, L_f, and L_g such that:

$$\|\mathbf{F}(s,\mathbf{x}(s);\mathbf{v}(s)) - \mathbf{F}(s,\mathbf{y}(s);\mathbf{v}(s))\|_1 \le L_0 \|\mathbf{x}(s) - \mathbf{y}(s)\|_1.$$

Using this Lipschitz estimate, we compute the difference for the operator:

$$\begin{aligned}
\|(\mathcal{T}\mathbf{x})(t) - (\mathcal{T}\mathbf{y})(t)\|_1 &\le \int_0^t \|\mathbf{F}(s,\mathbf{x}(s);\mathbf{v}(s)) - \mathbf{F}(s,\mathbf{y}(s);\mathbf{v}(s))\|_1 \, ds \\
&\le L_0 \int_0^t \|\mathbf{x}(s) - \mathbf{y}(s)\|_1 \, ds \\
&= L_0 \int_0^t e^{\lambda s}\left(e^{-\lambda s}\|\mathbf{x}(s) - \mathbf{y}(s)\|_1\right) ds \\
&\le L_0 \|\mathbf{x} - \mathbf{y}\|_\lambda \int_0^t e^{\lambda s} \, ds \le \frac{L_0}{\lambda} e^{\lambda t} \|\mathbf{x} - \mathbf{y}\|_\lambda.
\end{aligned}$$

Multiplying both sides by $e^{-\lambda t}$ and taking the supremum over $t \in [0,T]$, we obtain: $\|\mathcal{T}\mathbf{x} - \mathcal{T}\mathbf{y}\|_\lambda \le \alpha \|\mathbf{x} - \mathbf{y}\|_\lambda$ with $\alpha = L_0/\lambda$. By choosing $\lambda > L_0$, we have that $\alpha = L_0/\lambda < 1$, which proves that $\mathcal{T}$ is a strict contraction mapping on the complete Banach space $C([0,T];\mathbb{R}^3)$. By the Banach Fixed-Point Theorem, there exists a unique fixed point $\mathbf{x} \in C([0,T];\mathbb{R}^3)$ such that $\mathcal{T}\mathbf{x} = \mathbf{x}$, providing the unique continuous solution to the integral equation (18).

Invariance of the region $[0,N]^3$ *a posteriori.* Once the unique mathematical solution $\mathbf{x}(t)$ is established, we prove that it remains structurally trapped inside the biologically relevant region $[0,N]^3$ for all $t \in [0,T]$. First, since $f(0,x_2) = 0$ and $g(0) = 0$, by the mean value theorem we can express the non-linearities along the trajectory as $f(x_1,x_2) = x_1\Phi(x_1,x_2)$ and $g(x_1) = x_1\Psi(x_1)$ for bounded continuous functions Φ and Ψ. Substituting these into the first state component equation yields $x_1'(t) = -x_1(t)[\beta(t)\Phi(x_1,x_2) + u(t)\Psi(x_1)]$. Integrating this relation via an exponential integrating factor gives:

$$x_1(t) = s_0 \exp\left(-\int_0^t [\beta(s)\Phi(x_1(s),x_2(s)) + u(s)\Psi(x_1(s))]ds\right).$$

Since $s_0 \in [0, N]$, the exponential factor guarantees that $x_1(t) \geq 0$ for all $t \in [0, T]$. Similarly, using the fact that $f(x_1, 0) = 0$, the second component satisfies $x_2'(t) = x_2(t)\left[p\beta(t)\frac{f(x_1, x_2)}{x_2} - \gamma(t)\right]$, which yields the exponential representation

$$x_2(t) = i_0 \exp\left(\int_0^t [p\beta(s)\frac{f(x_1, x_2)}{x_2} - \gamma(s)]ds\right),$$

which implies that $x_2(t) \geq 0$ since $i_0 \in [0, N]$. Knowing that $x_1(t) \geq 0$ and $x_2(t) \geq 0$, the right-hand side of the third component satisfies $x_3'(t) = u(t)g(x_1) + (1-p)\beta(t)f(x_1, x_2) + \gamma(t)x_2 \geq 0$, which ensures $x_3(t) \geq r_0 \geq 0$. Furthermore, summing all components reveals the mass conservation law, $\sum_{i=1}^{3} F_i(t, \mathbf{x}; \mathbf{v}) = 0$, implying $x_1(t) + x_2(t) + x_3(t) = s_0 + i_0 + r_0 \leq N$. Since each component is non-negative, it follows directly that $x_i(t) \leq N$ for all $i \in \{1, 2, 3\}$. Therefore, the trajectory satisfies $\mathbf{x}(t) \in [0, N]^3$ uniformly on $[0, T]$, confirming that the global solution coincides exactly with the original Behncke non-linear dynamics without extensions.

To conclude that $\mathbf{x} \in W^{1,2}([0, T]; \mathbb{R}^3)$, we analyze the weak derivative $\mathbf{x}'(t)$. From the integral Equation (18), the fundamental theorem of calculus for the Lebesgue integral implies that $\mathbf{x}'(t) = \mathbf{F}(t, \mathbf{x}(t); \mathbf{v}(t))$ for almost every $t \in [0, T]$. Since $\mathbf{x}(t)$ is continuous on $[0, T]$, the terms $f(x_1(t), x_2(t))$ and $g(x_1(t))$ are continuous and bounded, meaning they belong to $L^\infty(0, T)$. The components of $\mathbf{F}(t, \mathbf{x}(t); \mathbf{v}(t))$ are linear combinations of products between the $L^\infty(0, T)$ state components and the $L^\infty(0, T) \subset L^2(0, T)$ admissible coefficients $\mathbf{v}$. Since the product of an L^2 function and an L^∞ function belongs to $L^2(0, T)$, it follows directly that each component of $\mathbf{x}'(t)$ is square-integrable, i.e., $\mathbf{x}' \in L^2([0, T]; \mathbb{R}^3)$. Combined with the continuity of $\mathbf{x}$, this formally proves that $\mathbf{x} \in W^{1,2}([0, T]; \mathbb{R}^3)$, completing the proof. □

3. Existence of Pareto-Optimal Solutions

In this section, we establish the existence of the weak Pareto-optimal solutions for the multi-objective optimization problem (11) and (12). To be more precise, we recall the notions of strictly and weakly efficient Pareto solutions [11,12]

Definition 1. *Let* $\mathbf{J} = (J_1, J_2, J_3)^T$ *be the objective vector defined in* (7)–(9) *under the notation* (14)–(17).

(i) *An admissible strategy* $\mathbf{v}^* \in \mathcal{U}_{ad}$ *is said to be a Pareto-optimal solution (or strictly efficient) of the multi-objective optimization problem* (11) *and* (12) *if and only if there does not exist another feasible strategy* $\mathbf{v} \in \mathcal{U}_{ad}$ *such that* $\mathcal{J}_k(\mathbf{v}) \leq \mathcal{J}_k(\mathbf{v}^*)$ *for all* $k \in \{1, 2, 3\}$, *and there exists at least one index* $m \in \{1, 2, 3\}$ *such that:* $\mathcal{J}_m(\mathbf{v}) < \mathcal{J}_m(\mathbf{v}^*)$.

(ii) *An admissible strategy* $\mathbf{v}^* \in \mathcal{U}_{ad}$ *is said to be a weak Pareto-optimal solution (or weakly efficient) if and only if there does not exist another feasible strategy* $\mathbf{v} \in \mathcal{U}_{ad}$ *such that:* $\mathcal{J}_k(\mathbf{v}) < \mathcal{J}_k(\mathbf{v}^*)$ *for all* $k \in \{1, 2, 3\}$.

Theorem 2. *Consider the notation* (14)–(17), *and* f *and* g *satisfying the assumptions* (1) *and* (2), *respectively. Suppose that* $\mathcal{U}_{ad}$ *is defined as in* (10), *the initial condition satisfies* $\mathbf{x}_0 \in [0, N]^3$, *and the experimental observations* $\mathbf{x}^{obs} \in L^2([0, T]; \mathbb{R}^3)$. *Then, there exists at least one weak Pareto-optimal strategy* $\mathbf{v}^* \in \mathcal{U}_{ad}$ *and its corresponding state* $\mathbf{x}^* \in W^{1,2}([0, T]; \mathbb{R}^3)$ *solving the multi-objective optimization problem* (11) *and* (12).

Proof. The methodology used to develop the proof is based on the generalized Karush–Kuhn–Tucker scalarization methodology for multi-objective optimization combined with

the direct method of the calculus of variations in reflexive Banach spaces. Let us introduce the scalarized optimization problem by defining the convex combination of the objectives:

$$\mathcal{J}_{\boldsymbol{\alpha}}(\mathbf{v}) = \sum_{i=1}^{3} \alpha_i \mathcal{J}_i(\mathbf{v}), \tag{21}$$

where $\boldsymbol{\alpha} = (\alpha_1, \alpha_2, \alpha_3)^T$ with $\alpha_i \geq 0$ for all $i \in \{1, 2, 3\}$ and $\sum_{i=1}^{3} \alpha_i = 1$. It is a well–established result in multi-objective optimization theory that any minimizer of the scalarized functional $\mathcal{J}_{\boldsymbol{\alpha}}$ over $\mathcal{U}_{\text{ad}}$ for strictly positive weights ($\alpha_i > 0$) corresponds to a strict Pareto-optimal solution, whereas non-negative weights ($\alpha_i \geq 0$) yield a weak Pareto-optimal point.

Let us fix a weight vector $\boldsymbol{\alpha}$ such that $\alpha_i \geq 0$. Since each individual cost functional $\mathcal{J}_i$ is non-negative, the scalarized objective function is bounded from below, implying that $d = \inf_{\mathbf{v} \in \mathcal{U}_{\text{ad}}} J_\alpha(\mathbf{v}) \geq 0$. Consequently, there exists a minimizing sequence $\mathbf{v}^n \in \mathcal{U}_{\text{ad}}$ such that:

$$\lim_{n \to \infty} \mathcal{J}_{\boldsymbol{\alpha}}(\mathbf{v}^n) = d. \tag{22}$$

The admissible set $\mathcal{U}_{\text{ad}}$ is a closed, bounded, and convex subset of the reflexive Banach space $L^2(0, T)^3$. By the Banach–Alaoglu Theorem, $\mathcal{U}_{\text{ad}}$ is weakly compact. Therefore, there exists a subsequence (still denoted by $\mathbf{v}^n$) and a limit vector $\mathbf{v}^* \in \mathcal{U}_{\text{ad}}$ such that $\mathbf{v}^n \rightharpoonup \mathbf{v}^*$ weakly in $L^2(0, T)^3$ as $n \to \infty$.

Let $\mathbf{x}^n \in W^{1,2}([0, T]; \mathbb{R}^3)$ be the unique solution to the state system (3)–(6) corresponding to $\mathbf{v}^n$. From Theorem II.1, the state solutions are uniformly bounded in $[0, N]^3$ for all $t \in [0, T]$. Taking the weak derivatives, we obtain:

$$\|\mathbf{x}^n\|_{W^{1,2}} = \|\mathbf{x}^n\|_{L^2} + \|(\mathbf{x}^n)'\|_{L^2} \leq C, \tag{23}$$

where $C > 0$ is a constant independent of n. This uniform bound implies that x^n is sequentially weakly compact in the Sobolev space $W^{1,2}([0, T]; \mathbb{R}^3)$. By the Rellich–Kondrachov theorem, the embedding $W^{1,2}([0, T]; \mathbb{R}^3) \subset\subset L^2([0, T]; \mathbb{R}^3)$ is compact. Furthermore, by the Sobolev embedding theorem combined with the Arzelà–Ascoli theorem, the embedding $W^{1,2}([0, T]; \mathbb{R}^3) \subset\subset C([0, T]; \mathbb{R}^3)$ is also compact. Thus, there exists a subsequence (still denoted by x^n) and a limit function $x^* \in C([0, T]; \mathbb{R}^3)$ such that $x^n \to x^*$ strongly in $C([0, T]; \mathbb{R}^3)$ as $n \to \infty$.

To show that the limit trajectory $\mathbf{x}^*$ satisfies the state equations governed by $\mathbf{v}^*$, we pass to the limit in the Volterra integral formulation (see (18)):

$$\mathbf{x}^n(t) = \mathbf{x}_0 + \int_0^t \mathbf{F}(s, \mathbf{x}^n(s); \mathbf{v}^n(s))\, ds. \tag{24}$$

Due to the strong convergence of the states in the continuous topology, the non-linearities satisfy $f(x_1^n, x_2^n) \to f(x_1^*, x_2^*)$ and $g(x_1^n) \to g(x_1^*)$ strongly in $C([0, T])$. Since the parameters converge weakly ($\mathbf{v}^n \rightharpoonup \mathbf{v}^*$ in $L^2(0, T)^3$), the product of a strongly convergent sequence and a weakly convergent sequence in $L^2(0, T)$ converges weakly to the product of their limits. Taking the limit as $n \to \infty$ on both sides of (24) yields:

$$\mathbf{x}^*(t) = \mathbf{x}_0 + \int_0^t \mathbf{F}(s, \mathbf{x}^*(s); \mathbf{v}^*(s))\, ds, \tag{25}$$

which confirms that $\mathbf{x}^* \in W^{1,2}([0, T]; \mathbb{R}^3)$ is the unique state solution associated with $\mathbf{v}^*$.

Finally, we analyze the lower semi-continuity of the cost functional $\mathcal{J}_{\boldsymbol{\alpha}}$. Since $\mathbf{x}^{\text{obs}} \in L^2([0, T]; \mathbb{R}^3)$, the functional $J_1(\mathbf{x}) = \frac{1}{2}\|\mathbf{x} - \mathbf{x}^{\text{obs}}\|_{L^2}^2$ is a shifted norm in an L^2 Hilbert space. Because any continuous convex functional on a Hilbert space is sequentially weakly lower semi-continuous, the strong convergence $\mathbf{x}^n \to \mathbf{x}^*$ in $C([0, T]; \mathbb{R}^3) \subset L^2([0, T]; \mathbb{R}^3)$ implies that $\liminf_{n \to \infty} J_1(\mathbf{x}^n) \geq J_1(\mathbf{x}^*)$. Similarly, J_2 is linear and continuous with respect to the state variable $x_2(t)$ in the strong topology of continuous functions, which preserves

exact convergence. For the vaccination control cost J_3, since $v_3 \mapsto \int_0^T v_3(t)\,dt$ is a linear and continuous functional on $L^2(0,T)$, it is sequentially weakly lower semi-continuous under the weak convergence $v_3^n \rightharpoonup v_3^*$. Combining these weak lower semi-continuity results across all three objectives and using (22), we obtain

$$d \leq \mathcal{J}_{\boldsymbol{\alpha}}(\mathbf{v}^*) \leq \liminf_{n\to\infty} \mathcal{J}_{\boldsymbol{\alpha}}(\mathbf{v}^n) = d, \tag{26}$$

which proves that $\mathcal{J}_{\boldsymbol{\alpha}}(\mathbf{v}^*) = d$. Hence, $\mathbf{v}^*$ is an optimal solution minimizing the scalarized objective, which guarantees that it constitutes a weak Pareto-optimal solution to the problem (11) and (12). □

Remark 1. *The existence result established in Theorem 2 guarantees the attainment of a weak Pareto-optimal solution because the scalarization weight vector is chosen within the non-negative orthant, i.e., $\alpha_i \geq 0$ for all $i \in \{1,2,3\}$. From a theoretical perspective, two structural considerations must be emphasized:*

(a) *Setting non-negative weights ($\alpha_i \geq 0$) analytically ensures weak Pareto efficiency, allowing the framework to incorporate boundary configurations (for instance, setting $\alpha_2 = \alpha_3 = 0$ to focus exclusively on the parameter identification problem J_1). If the weights are restricted to be strictly positive ($\alpha_i > 0$ for all i), any minimizer of (21) constitutes a strict Pareto-optimal solution of the multi-objective problem (11) (see, for instance, Ref. [12]).*

(b) *Because the underlying compartmental epidemic dynamics (17) are inherently non-linear, global convexity of the reachable objective set $\mathcal{J}(\mathcal{U}_{ad})$ cannot be guaranteed a priori. Consequently, the weighted-sum approach implemented in (21) is mathematically capable of tracing only the convexly supported portion of the Pareto set. Any non-convex segments or local efficiency gaps along the true Pareto front fall outside the scope of linear scalarization, meaning that the numerical boundaries approximated in Section 6 strictly represent this supported Pareto envelope.*

4. Dubovitskii–Milyutin Formalism Notation and Results

In this section, we introduce the appropriate notation used Dubovitskii–Milyutin formalism. In particular, we establish the required differentiability properties, which enable the construction of the descent and tangent cones along with their respective duals.

Let us introduce the notation. The state and control functional spaces are denoted by

$$E = W^{1,2}([0,T];\mathbb{R}^3) \times L^2(0,T)^3, \tag{27}$$

$$\tilde{E} = L^2(0,T)^3 \times \mathbb{R}^3. \tag{28}$$

In the context of the notation (14)–(17) and considering that

$$\boldsymbol{\psi}(t) = \Big(\psi_1(t), \psi_2(t), \psi_3(t)\Big)^\top, \boldsymbol{\xi} = (\xi_1, \xi_2, \xi_3), \tag{29}$$

we define the constraint operator $\mathcal{M} : E \to \tilde{E}$ by the following relation

$$\mathcal{M}(\mathbf{x}, \mathbf{v}) = (\boldsymbol{\psi}, \boldsymbol{\xi}), \tag{30}$$

if and only if

$$\mathbf{x}'(t) - \mathbf{F}(t, \mathbf{x}; \mathbf{v}) = \boldsymbol{\psi}, \quad \mathbf{x}(0) - \mathbf{x}_0 = \boldsymbol{\xi}. \tag{31}$$

Furthermore, we define the feasible set $\mathcal{D} \subset E$ as the kernel of the operator $\mathcal{M}$, which encapsulates the dynamic and initial state configurations, namely:

$$\mathcal{D} = \Big\{(\mathbf{x}, \mathbf{v}) \in E \ : \ \mathcal{M}(\mathbf{x}, \mathbf{v}) = \mathbf{0}_{\tilde{E}}\Big\}. \tag{32}$$

In the context of this functional framework, the multi-objective optimization problem (11) and (12) can be rewritten in a compact abstract form as follows:

$$\text{Minimize } \mathbf{J}(\mathbf{x}, \mathbf{v}), \tag{33}$$

$$\text{subject to } (\mathbf{x}, \mathbf{v}) \in \mathcal{D} \cap \Big(W^{1,2}([0,T]; \mathbb{R}^3) \times \mathcal{U}_{\text{ad}} \Big). \tag{34}$$

Here, we introduce two key observations. First, the abstract formulation (33) and (34) is formally consistent since the structural operator $\mathcal{M}$ is well-defined, and the core epidemiological system (3)–(6) represents a particular case of the general perturbed equations (31) when $\boldsymbol{\psi}(t) = 0$ and $\boldsymbol{\xi} = 0$. Consequently, the well-posedness of the perturbed system (31) can be readily deduced by applying a mathematical methodology analogous to the one detailed in Section 2. Second, expressing the cost vector as $\mathbf{J}(\mathbf{x}, \mathbf{v})$ is a formal shorthand introduced to explicitly emphasize the dependency of the state variables on the choice of the control and parameter tuple. While the objective functions structurally depend only on the state variable and the vaccination effort, each state variables is uniquely and implicitly determined by the configuration of $\mathbf{v}$ through the kernel constraint $\mathcal{M}(\mathbf{x}, \mathbf{v}) = \mathbf{0}_{\tilde{E}}$.

Lemma 1. *Consider the notation (14)–(17) and (27)–(34); f and g satisfying the assumptions (1) and (2), respectively; $\mathcal{U}_{ad}$ defined by (10); $\mathbf{x}_0 \in [0,N]^3$; $\mathbf{x}^{obs} \in L^2([0,T];\mathbb{R}^3)$; and the objective functionals J_1, J_2, and J_3 defined in (7) and (8) and the constraint operator $\mathcal{M}$ defined by (30) and (31). Then, the cost functionals J_1, J_2, and J_3 are Fréchet differentiable on E. Their respective Fréchet derivatives at the point $(\mathbf{x}, \mathbf{v}) \in E$ in the direction of the perturbation $(\tilde{\mathbf{x}}, \tilde{\mathbf{v}}) \in E$ are given by:*

$$J_1'(\mathbf{x}, \mathbf{v})(\tilde{\mathbf{x}}, \tilde{\mathbf{v}}) = \int_0^T \Big(\mathbf{x}(t) - \mathbf{x}^{obs}(t) \Big) \cdot \tilde{\mathbf{x}}(t) dt \tag{35}$$

$$J_2'(\mathbf{x}, \mathbf{v})(\tilde{\mathbf{x}}, \tilde{\mathbf{v}}) = \int_0^T \tilde{x}_2(t)\, dt, \tag{36}$$

$$J_3'(\mathbf{x}, \mathbf{v})(\tilde{\mathbf{x}}, \tilde{\mathbf{v}}) = \int_0^T \tilde{v}_3(t)\, dt. \tag{37}$$

Moreover, the descent cones K_{d_i} for $i \in \{1,2,3\}$ are convex and open sets given by

$$K_{d_i} = \Big\{ (\tilde{\mathbf{x}}, \tilde{\mathbf{v}}) \in E \ : \ J_i'(\mathbf{x}, \mathbf{v})(\tilde{\mathbf{x}}, \tilde{\mathbf{v}}) < 0 \Big\}, \tag{38}$$

and their corresponding dual cones $K_{d_i}^* \subset E^*$ are characterized by the sets:

$$K_{d_i}^* = \Big\{ f_i \in E^* \ : \ f_i(\tilde{\mathbf{x}}, \tilde{\mathbf{v}}) = -\lambda_i J_i'(\mathbf{x}, \mathbf{v})(\tilde{\mathbf{x}}, \tilde{\mathbf{v}}),\ \lambda_i \geq 0 \Big\}. \tag{39}$$

Proof. We divide the proof into three parts, establishing the differentiability of each functional and deriving their cones.

The proof of the Fréchet differentiability can be developed as follows. Let $(\mathbf{x}, \mathbf{v}) \in E$ and let $(\tilde{\mathbf{x}}, \tilde{\mathbf{v}}) \in E$ be a small perturbation. For J_1, we have that

$$\begin{aligned} &J_1\Big((\mathbf{x}, \mathbf{v}) + (\tilde{\mathbf{x}}, \tilde{\mathbf{v}}) \Big) - J_1(\mathbf{x}, \mathbf{v}) \\ &= \frac{1}{2}\Big[\|\mathbf{x} + \tilde{\mathbf{x}} - \mathbf{x}^{\text{obs}}\|^2_{L^2(0,T)} - \|\mathbf{x} - \mathbf{x}^{\text{obs}}\|^2_{L^2(0,T)} \Big] \\ &= \int_0^T \Big(\mathbf{x}(t) - \mathbf{x}^{\text{obs}}(t) \Big) \cdot \tilde{\mathbf{x}}(t) dt + \frac{1}{2}\|\tilde{\mathbf{x}}\|^2_{L^2(0,T)}. \end{aligned}$$

Let us define the linear functional $L_1(\tilde{\mathbf{x}}, \tilde{\mathbf{v}})$ as the first integral expression, which is clearly continuous on E due to the Cauchy–Schwarz inequality. The second term satisfies the condition

$$\lim_{\|(\tilde{\mathbf{x}}, \tilde{\mathbf{v}})\|_E \to 0} \frac{\frac{1}{2}\|\tilde{\mathbf{x}}\|^2_{L^2}}{\|(\tilde{\mathbf{x}}, \tilde{\mathbf{v}})\|_E} \leq \lim_{\|\tilde{\mathbf{w}}\|_E \to 0} \frac{1}{2}\|(\tilde{\mathbf{x}}, \tilde{\mathbf{v}})\|_E = 0, \tag{40}$$

where we used the continuous embedding $W^{1,2}([0,T];\mathbb{R}^3) \hookrightarrow L^2(0,T)^3$. This formally proves that J_1 is Fréchet differentiable with derivative $J_1'(\mathbf{x},\mathbf{v}) = L_1(\tilde{\mathbf{x}},\tilde{\mathbf{v}})$, confirming the (35). For the cost functionals J_2 and J_3, we observe that they are linear bounded functionals with respect to their arguments $x_2(t)$ and $v_3(t)$ in $L^2(0,T)$ or $W^{1,2}([0,T])$. Since any bounded linear operator is trivially equal to its own Fréchet derivative, we have:

$$\begin{aligned} &J_2\Big((\mathbf{x},\mathbf{v}) + (\tilde{\mathbf{x}},\tilde{\mathbf{v}})\Big) - J_2(\mathbf{x},\mathbf{v}) \\ &\quad = \int_0^T (x_2(t) + \tilde{x}_2(t))\,dt - \int_0^T x_2(t)\,dt = \int_0^T \tilde{x}_2(t)\,dt, \\ &J_3\Big((\mathbf{x},\mathbf{v}) + (\tilde{\mathbf{x}},\tilde{\mathbf{v}})\Big) - J_3(\mathbf{x},\mathbf{v}) \\ &\quad = \int_0^T (v_3(t) + \tilde{v}_3(t))\,dt - \int_0^T v_3(t)\,dt = \int_0^T \tilde{v}_3(t)\,dt. \end{aligned}$$

Hence, the linear operators in (36) and (37) constitute the exact Fréchet derivatives of J_2 and J_3, respectively.

The characterization of the descent cones is developed as follows. According to the Dubovitskii–Milyutin optimization theory, the cone of descent directions K_d for a Fréchet differentiable functional J is defined as the set of all directions along which the functional strictly decreases. Since the derivatives $J_i'(\mathbf{x},\mathbf{v})$ are continuous linear functionals, the mapping $(\tilde{\mathbf{x}},\tilde{\mathbf{v}}) \mapsto J_i'(\mathbf{x},\mathbf{v})(\tilde{\mathbf{x}},\tilde{\mathbf{v}})$ is inherently continuous. Consequently, the set $K_{d_i} = \Big\{(\tilde{\mathbf{x}},\tilde{\mathbf{v}}) \in E : J_i'(\mathbf{x},\mathbf{v})(\tilde{\mathbf{x}},\tilde{\mathbf{v}}) < 0\Big\}$ is the inverse image of the open interval $(-\infty, 0)$ under a continuous map, which implies that K_{d_i} is an open set. Furthermore, if $(\tilde{\mathbf{x}}_1,\tilde{\mathbf{v}}_1), (\tilde{\mathbf{x}}_2,\tilde{\mathbf{v}}_2) \in K_{d_i}$ and $\theta \in [0,1]$, the linearity of the derivative guarantees

$$\begin{aligned} &J_i'(\mathbf{x},\mathbf{v})\Big(\theta(\tilde{\mathbf{x}}_1,\tilde{\mathbf{v}}_1) + (1-\theta)(\tilde{\mathbf{x}}_2,\tilde{\mathbf{v}}_2)\Big) \\ &\quad = \theta J_i'(\mathbf{x},\mathbf{v})(\tilde{\mathbf{x}}_1,\tilde{\mathbf{v}}_1) + (1-\theta)J_i'(\mathbf{x},\mathbf{v})(\tilde{\mathbf{x}}_2,\tilde{\mathbf{v}}_2) < 0, \end{aligned}$$

which establishes the convexity of the descent cones. Hence, we deduce the relation (38) and its convexity.

Finally, for characterization of the dual cones we proceed as follows. By definition, the dual cone K^* of any cone $K \subset E$ is the set of all continuous linear functionals $f \in E^*$ that are non-negative on K, i.e.,

$$K^* = \Big\{l \in E^* : l(\tilde{\mathbf{x}},\tilde{\mathbf{v}}) \geq 0, \quad \forall (\tilde{\mathbf{x}},\tilde{\mathbf{v}}) \in K\Big\}.$$

From (38), the dual cone consists precisely of the negative half-lines generated by the linear functional L. Then, setting $L = J_i'(\mathbf{w})$, we immediately obtain (39), which concludes the proof of the lemma. □

Lemma 2. *Assume that the hypotheses of Lemma 1 are satisfied. Let the Jacobian matrices with respect to the state and parameter–control variables be defined respectively by:*

$$D_{\mathbf{x}}\mathbf{F} = \begin{pmatrix} -v_1\partial_1 f(x_1,x_2) - v_3 g'(x_1) & -v_1\partial_2 f(x_1,x_2) & 0 \\ pv_1\partial_1 f(x_1,x_2) & pv_1\partial_2 f(x_1,x_2) - v_2 & 0 \\ v_3 g'(x_1) + (1-p)v_1\partial_1 f(x_1,x_2) & (1-p)v_1\partial_2 f(x_1,x_2) + v_2 & 0 \end{pmatrix},$$

$$D_{\mathbf{v}}\mathbf{F} = \begin{pmatrix} -f(x_1,x_2) & 0 & -g(x_1) \\ pf(x_1,x_2) & -x_2 & 0 \\ (1-p)f(x_1,x_2) & x_2 & g(x_1) \end{pmatrix}.$$

Then, the constraint operator $\mathcal{M}$ defined in (30) and (31) is Fréchet differentiable on E. Its Fréchet derivative $\mathcal{M}'(\mathbf{x},\mathbf{v})(\tilde{\mathbf{x}},\tilde{\mathbf{v}}) = (\tilde{\boldsymbol{\psi}},\tilde{\boldsymbol{\xi}})^\top \in \tilde{E}$ at the point $(\mathbf{x},\mathbf{v}) \in E$ along the perturbation direction $(\tilde{\mathbf{x}},\tilde{\mathbf{v}}) \in E$ is uniquely determined by the solution of the following compact linearized system:

$$\tilde{\mathbf{x}}'(t) - D_{\mathbf{x}}\mathbf{F}(t,\mathbf{x};\mathbf{v})\tilde{\mathbf{x}}(t) - D_{\mathbf{v}}\mathbf{F}(t,\mathbf{x};\mathbf{v})\tilde{\mathbf{v}}(t) = \tilde{\boldsymbol{\psi}}(t), \tag{41}$$

$$\tilde{\mathbf{x}}(0) = \tilde{\boldsymbol{\xi}}, \tag{42}$$

where $\tilde{\boldsymbol{\psi}}(t) \in L^2(0,T)^3$ *and* $\tilde{\boldsymbol{\xi}} \in \mathbb{R}^3$.

Proof. To establish the Fréchet differentiability of the constraint operator $\mathcal{M} : E \to \tilde{E}$, we must demonstrate that the operator increment can be decomposed into a continuous linear mapping plus a higher-order remainder term that vanishes in the topology of the target space $\tilde{E}$. Let us define the mapping $\mathcal{L}(\tilde{\mathbf{x}}, \tilde{\mathbf{v}})$ as the left-hand side of the compact linearized system (41) and (42), which is clearly linear with respect to the perturbation pair $(\tilde{\mathbf{x}}, \tilde{\mathbf{v}})$.

By using the compact vector notation, the algebraic expansion of the operator increment evaluated at the perturbed states and parameters can be written in a structured block form as:

$$\begin{aligned} &\mathcal{M}(\mathbf{x}+\tilde{\mathbf{x}}, \mathbf{v}+\tilde{\mathbf{v}}) - \mathcal{M}(\mathbf{x}, \mathbf{v}) \\ &= \begin{pmatrix} (\mathbf{x}' + \tilde{\mathbf{x}}') - \mathbf{F}(t, \mathbf{x}+\tilde{\mathbf{x}}; \mathbf{v}+\tilde{\mathbf{v}}) \\ (\mathbf{x}(0) + \tilde{\mathbf{x}}(0)) - \mathbf{x}_0 \end{pmatrix} - \begin{pmatrix} \mathbf{x}' - \mathbf{F}(t, \mathbf{x}; \mathbf{v}) \\ \mathbf{x}(0) - \mathbf{x}_0 \end{pmatrix}. \end{aligned} \tag{43}$$

By applying the linearity of the weak differential operator and canceling the homogeneous initial population vector $\mathbf{x}_0$, expression (43) simplifies directly to:

$$\begin{aligned} &\mathcal{M}(\mathbf{x}+\tilde{\mathbf{x}}, \mathbf{v}+\tilde{\mathbf{v}}) - \mathcal{M}(\mathbf{x}, \mathbf{v}) \\ &\qquad = \begin{pmatrix} \tilde{\mathbf{x}}'(t) - \left[\mathbf{F}(t, \mathbf{x}+\tilde{\mathbf{x}}; \mathbf{v}+\tilde{\mathbf{v}}) - \mathbf{F}(t, \mathbf{x}; \mathbf{v}) \right] \\ \tilde{\mathbf{x}}(0) \end{pmatrix}. \end{aligned} \tag{44}$$

From the assumptions (1) and (2), where $f \in C^2([0,N]^2, \mathbb{R})$ and $g \in C^1([0,N], \mathbb{R})$, we deduce that the structural vector field $\mathbf{F}$ is continuously differentiable with respect to both its state and parameter arguments on their compact domains. Consequently, we expand the non-linear field vector using the multivariate Taylor's theorem around the solution $(\mathbf{x}, \mathbf{v})$, which yields the identity

$$\begin{aligned} \mathbf{F}(t, \mathbf{x}+\tilde{\mathbf{x}}; \mathbf{v}+\tilde{\mathbf{v}}) &= \mathbf{F}(t, \mathbf{x}; \mathbf{v}) \\ &+ D_{\mathbf{x}}\mathbf{F}(t, \mathbf{x}; \mathbf{v})\tilde{\mathbf{x}}(t) + D_{\mathbf{v}}\mathbf{F}(t, \mathbf{x}; \mathbf{v})\tilde{\mathbf{v}}(t) + \mathcal{R}_{\mathbf{F}}(\tilde{\mathbf{x}}, \tilde{\mathbf{v}}), \end{aligned} \tag{45}$$

where $D_{\mathbf{x}}\mathbf{F}$ and $D_{\mathbf{v}}\mathbf{F}$ are the Jacobian matrices, and $\mathcal{R}_{\mathbf{F}}(\tilde{\mathbf{x}}, \tilde{\mathbf{v}}) \in \mathbb{R}^3$ represents the higher-order Taylor remainder vector containing cross-multiplications of the perturbations. Substituting (45) into the block increment relation (44), we obtain:

$$\begin{aligned} &\mathcal{M}(\mathbf{x}+\tilde{\mathbf{x}}, \mathbf{v}+\tilde{\mathbf{v}}) - \mathcal{M}(\mathbf{x}, \mathbf{v}) \\ &= \begin{pmatrix} \tilde{\mathbf{x}}'(t) - D_{\mathbf{x}}\mathbf{F}(t, \mathbf{x}; \mathbf{v})\tilde{\mathbf{x}}(t) - D_{\mathbf{v}}\mathbf{F}(t, \mathbf{x}; \mathbf{v})\tilde{\mathbf{v}}(t) - \mathcal{R}_{\mathbf{F}}(\tilde{\mathbf{x}}, \tilde{\mathbf{v}}) \\ \tilde{\mathbf{x}}(0) \end{pmatrix} \\ &= \mathcal{M}'(\mathbf{x}, \mathbf{v})(\tilde{\mathbf{x}}, \tilde{\mathbf{v}}) - \begin{pmatrix} \mathcal{R}_{\mathbf{F}}(\tilde{\mathbf{x}}, \tilde{\mathbf{v}}) \\ \mathbf{0}_{\mathbb{R}^3} \end{pmatrix}. \end{aligned} \tag{46}$$

Using the linearized definitions from (41) and (42), the system satisfies $\mathcal{M}'(\mathbf{x}, \mathbf{v})(\tilde{\mathbf{x}}, \tilde{\mathbf{v}}) = (\tilde{\boldsymbol{\psi}}, \tilde{\boldsymbol{\xi}})^\top \in \tilde{E}$. To formally prove that this continuous linear mapping constitutes the true Fréchet derivative of $\mathcal{M}$, we must verify that the remaining Taylor residue vanishes faster than the perturbation norm in the product topology of $\tilde{E} = L^2(0,T)^3 \times \mathbb{R}^3$.

By employing the Cauchy–Schwarz inequality, the fact that the state and parameter domains are bounded in $L^\infty(0,T)$, and the continuous Sobolev embedding $W^{1,2}([0,T]; \mathbb{R}^3) \hookrightarrow C([0,T]; \mathbb{R}^3)$, every individual term within the remainder vector $\mathcal{R}_{\mathbf{F}}(\tilde{\mathbf{x}}, \tilde{\mathbf{v}})$ is bounded from above by a quadratic functionality of the perturbations. Specifically, there exists a positive embedding constant $C_0 > 0$ such that

$$\begin{aligned} &\|\mathcal{R}_{\mathbf{F}}(\tilde{\mathbf{x}}, \tilde{\mathbf{v}})\|_{L^2(0,T)^3} \\ &\quad \le C_0 \left(\|\tilde{\mathbf{x}}\|^2_{C([0,T])^3} + \|\tilde{\mathbf{x}}\|_{C([0,T])^3} \|\tilde{\mathbf{v}}\|_{L^2(0,T)^3} \right) \\ &\quad \le C_0 \|(\tilde{\mathbf{x}}, \tilde{\mathbf{v}})\|^2_{\tilde{E}}. \end{aligned}$$

Taking the limit as the perturbation norm approaches zero in the Sobolev space E, we obtain:

$$\lim_{\|(\tilde{\mathbf{x}},\tilde{\mathbf{v}})\|_E\to 0} \frac{\left\| \begin{pmatrix} \delta\mathcal{R}_{\mathbf{F}}(\tilde{\mathbf{x}},\tilde{\mathbf{v}}) \\ \mathbf{0}_{\mathbb{R}^3} \end{pmatrix} \right\|_{\tilde{E}}}{\|(\tilde{\mathbf{x}},\tilde{\mathbf{v}})\|_E} \leq \lim_{\|(\tilde{\mathbf{x}},\tilde{\mathbf{v}})\|_E\to 0} C_0 \|(\tilde{\mathbf{x}},\tilde{\mathbf{v}})\|_E = 0.$$

This confirms that the remainder vanishes in accordance with Fréchet's requirements. Since the linear operator $\mathcal{M}'(\mathbf{x},\mathbf{v})$ is bounded from E into $\tilde{E}$ due to the boundedness of the Jacobian entries on the compact trajectories, we conclude that $\mathcal{M}$ is Fréchet differentiable and its derivative is uniquely determined by the system (41) and (42), which completes the proof. □

Lemma 3. *Assume that the hypotheses of Lemma 1 are satisfied. Then, the constraint operator $\mathcal{M}$ defined in (30) and (31) is strictly differentiable on E, and its linear derivative $\mathcal{M}'(\mathbf{x},\mathbf{v}) : E \to \tilde{E}$ is a surjective operator.*

Proof. The strict differentiability of the constraint operator $\mathcal{M}$ follows directly from the fact that its Fréchet derivative $\mathcal{M}'(\mathbf{x},\mathbf{v})$, established in Lemma 2, is continuous with respect to the base point $(\mathbf{x},\mathbf{v})$ in the operator norm topology. This continuity is a direct analytical consequence of the continuous differentiability (C^2) of the Behncke-type structural nonlinear functionalities f and g on their respective compact domains.

To establish the surjectivity of the linear operator $\mathcal{M}'(\mathbf{x},\mathbf{v}) : E \to \tilde{E}$, we must prove that for every arbitrary target perturbation vector $(\tilde{\boldsymbol{\psi}},\tilde{\boldsymbol{\xi}})^\top \in \tilde{E}$, there exists at least one feasible direction pair $(\tilde{\mathbf{x}},\tilde{\mathbf{v}})^\top \in E$ satisfying the operator relation:

$$\mathcal{M}'(\mathbf{x},\mathbf{v})(\tilde{\mathbf{x}},\tilde{\mathbf{v}}) = (\tilde{\boldsymbol{\psi}},\tilde{\boldsymbol{\xi}})^\top. \tag{47}$$

A highly elegant and direct approach to construct such a preimage is to restrict our choice within the control space by setting the parameter and vaccination variations to zero, namely $\tilde{\mathbf{v}}(t) = \mathbf{0}_{L^2}$ for almost every $t \in [0,T]$. By substituting this homogeneous vector into the compact linearized system (41) and (42), the parameter Jacobian term vanishes identically, and the problem reduces to finding a state perturbation vector $\tilde{\mathbf{x}}(t) \in W^{1,2}([0,T];\mathbb{R}^3)$ satisfying

$$\tilde{\mathbf{x}}'(t) - D_{\mathbf{x}}\mathbf{F}(t,\mathbf{x};\mathbf{v})\tilde{\mathbf{x}}(t) = \tilde{\boldsymbol{\psi}}(t), \quad \tilde{\mathbf{x}}(0) = \tilde{\boldsymbol{\xi}}, \tag{48}$$

subject to the exact initial vector condition: where $\tilde{\boldsymbol{\psi}}_L \in L^2(0,T)^3$ represents the nonhomogeneous target perturbation vector.

Since the base state trajectory $\mathbf{x}(t)$ is continuous on the compact interval $[0,T]$, the underlying partial derivatives evaluated within the state Jacobian matrix $D_{\mathbf{x}}\mathbf{F}(t,\mathbf{x};\mathbf{v})$ are continuous and globally bounded. Furthermore, because the base parameter configuration satisfies $\mathbf{v}(t) \in \mathcal{U}_{\text{ad}} \subset L^\infty(0,T)^3$, every individual entry of the matrix $D_{\mathbf{x}}\mathbf{F}(t,\mathbf{x};\mathbf{v})$ belongs to $L^\infty(0,T)$, implying that $D_{\mathbf{x}}\mathbf{F} \in L^\infty(0,T)^{3\times 3} \subset L^1(0,T)^{3\times 3}$.

According to the classical existence and uniqueness theory for linear ordinary differential equations with integrable coefficients (the Carathéodory existence theorem), since $D_{\mathbf{x}}\mathbf{F} \in L^1(0,T)^{3\times 3}$ and the source vector satisfies [23] $\tilde{\boldsymbol{\psi}} \in L^2(0,T)^3 \subset L^1(0,T)^3$, for any given initial data vector $\tilde{\boldsymbol{\xi}} \in \mathbb{R}^3$, there exists a unique absolutely continuous solution $\tilde{\mathbf{x}}(t)$ satisfying (48) for almost every $t \in [0,T]$.

To verify that this unique solution possesses the required Sobolev regularity, we isolate the derivative term from the matrix relation: $\tilde{\mathbf{x}}'(t) = \tilde{\boldsymbol{\psi}}_L(t) + D_{\mathbf{x}}\mathbf{F}(t,\mathbf{x};\mathbf{v})\tilde{\mathbf{x}}(t)$. Since $\tilde{\mathbf{x}}(t)$ is continuous on the compact interval $[0,T]$, it is bounded and belongs to $L^\infty(0,T)^3$. Given that $D_{\mathbf{x}}\mathbf{F} \in L^\infty(0,T)^{3\times 3}$, the matrix-vector product satisfies $D_{\mathbf{x}}\mathbf{F}\tilde{\mathbf{x}} \in L^\infty(0,T)^3 \subset L^2(0,T)^3$. Knowing that $\tilde{\boldsymbol{\psi}}_L \in L^2(0,T)^3$, the linear combination of two L^2 functions yields $\tilde{\mathbf{x}}' \in L^2([0,T];\mathbb{R}^3)$. Therefore, $\tilde{\mathbf{x}} \in W^{1,2}([0,T];\mathbb{R}^3)$, which validates that $(\tilde{\mathbf{x}},\mathbf{0}_{L^2})^\top \in E$.

Consequently, the constructed choice $(\tilde{\mathbf{x}}, \mathbf{0}_{L^2})^\top \in E$ satisfies the operator relation $\mathcal{M}'(\mathbf{x}, \mathbf{v})(\tilde{\mathbf{x}}, \mathbf{0}_{L^2}) = (\tilde{\boldsymbol{\psi}}, \tilde{\boldsymbol{\xi}})^\top$ exactly. This formally proves that every arbitrary element in the target space $\tilde{E}$ possesses a valid preimage in E, which certifies that the linear derivative operator $\mathcal{M}'(\mathbf{x}, \mathbf{v})$ is surjective, completing the proof of the lemma. □

Lemma 4. *Assume that the hypotheses of Lemma 1 are satisfied. Then, the tangent cone K_T to the feasible constraint set $\mathcal{D}$ at the point $(\mathbf{x}, \mathbf{v})$ and its closed dual cone $K_T^* \subset E^*$ are given by:*

$$K_T = \left\{ (\tilde{\mathbf{x}}, \tilde{\mathbf{v}}) \in E \ : \ \mathcal{M}'(\mathbf{x}, \mathbf{v})(\tilde{\mathbf{x}}, \tilde{\mathbf{v}}) = \mathbf{0}_{\tilde{E}} \right\}, \tag{49}$$

$$K_T^* = \left\{ \mathcal{L} \in E^* \ : \ \mathcal{L}(\tilde{\mathbf{x}}, \tilde{\mathbf{v}}) = 0, \quad \forall (\tilde{\mathbf{x}}, \tilde{\mathbf{v}}) \in K_T \right\}. \tag{50}$$

Additionally, K_T forms a closed vector subspace of E.

Proof. We divide the proof into two steps, first justifying the algebraic representation of the tangent cone through Lyusternik's Theorem and subsequently characterizing its dual structure.

The algebraic representation of the tangent cone is developed as follows. According to the Dubovitskii–Milyutin optimization framework, the tangent cone to a set defined strictly by operator equalities of the form $\mathcal{D} = \{(\mathbf{x}, \mathbf{v}) \in E : \mathcal{M}(\mathbf{x}, \mathbf{v}) = \mathbf{0}_{\tilde{E}}\}$ is not guaranteed to coincide with the kernel of the derivative unless the constraint operator satisfies specific regular conditions. By Lemma 3, the operator $\mathcal{M}$ is strictly differentiable at $(\mathbf{x}, \mathbf{v})$ and its linear Fréchet derivative $\mathcal{M}'(\mathbf{x}, \mathbf{v}) : E \to \tilde{E}$ is a surjective mapping between the Banach spaces E and $\tilde{E}$. Under these exact conditions, we invoke the classical Lyusternik Theorem (or the Generalized Inverse Function Theorem) [24], which states that the tangent cone to the kernel of a regular operator is precisely the kernel of its derivative. This establishes the validity of the set identity defined in (49). Furthermore, since $\mathcal{M}'(\mathbf{x}, \mathbf{v})$ is a bounded linear operator, its kernel is the inverse image of the closed singleton $\{\mathbf{0}_{\tilde{E}}\}$. Consequently, $K_T = \ker(\mathcal{M}'(\mathbf{x}, \mathbf{v}))$ is a closed subset under the norm topology of E. Since the kernel of any linear operator preserves vector addition and scalar multiplication, K_T constitutes a closed vector subspace of E.

The characterization of the tangent cone is developed as follows. By definition, the dual cone K^* of a subset $K \subset E$ within the functional framework of Dubovitskii–Milyutin is defined as the set of continuous linear functionals supporting the geometry of K, namely, $K^* = \{\mathcal{L} \in E^* : \mathcal{L}(\tilde{\mathbf{x}}, \tilde{\mathbf{v}}) \geq 0, \ \forall (\tilde{\mathbf{x}}, \tilde{\mathbf{v}}) \in K\}$. Since we have proven that the tangent cone K_T is a vector subspace of E, it possesses the property of symmetry under sign inversion; that is, if $(\tilde{\mathbf{x}}, \tilde{\mathbf{v}}) \in K_T$, then $-(\tilde{\mathbf{x}}, \tilde{\mathbf{v}}) \in K_T$. Let $\mathcal{L} \in K_T^*$. Then, by definition of the dual cone, the functional must satisfy the inequality $\mathcal{L}(\tilde{\mathbf{x}}, \tilde{\mathbf{v}}) \geq 0$ for all $(\tilde{\mathbf{x}}, \tilde{\mathbf{v}}) \in K_T$. Substituting the symmetric element $-(\tilde{\mathbf{x}}, \tilde{\mathbf{v}}) \in K_T$ into the functional relation yields $\mathcal{L}(-(\tilde{\mathbf{x}}, \tilde{\mathbf{v}})) \geq 0$, which by linearity implies $-\mathcal{L}(\tilde{\mathbf{x}}, \tilde{\mathbf{v}}) \geq 0$, or equivalently, $\mathcal{L}(\tilde{\mathbf{x}}, \tilde{\mathbf{v}}) \leq 0$. To satisfy both inequalities simultaneously, the continuous linear functional must vanish identically over the entire subspace. Thus, we have: $\mathcal{L}(\tilde{\mathbf{x}}, \tilde{\mathbf{v}}) = 0$ for all $(\tilde{\mathbf{x}}, \tilde{\mathbf{v}}) \in K_T$. This indicates that the dual cone of a vector subspace is its orthogonal annihilator $K_T^\perp \subset E^*$, which formally confirms the structural formulation provided in (50) and completes the proof. □

5. First-Order Optimality Conditions

In this section, we derive the first-order necessary optimality conditions for the multi-objective optimization problem (11) and (12) by applying the Dubovitskii–Milyutin formalism to the abstract formulation (33) and (34). To this end, we begin by defining the adjoint system. Then, based on the geometric structures introduced in the previous section, we state the formal first-order optimality conditions.

Lemma 5. *Assume that the hypotheses of Lemma 1 are satisfied and considering the notation of Jacobian matrices defined in the enunciate of Lemma 2. For any given scalarization weight vector* $\boldsymbol{\alpha} = (\alpha_1, \alpha_2, \alpha_3)^\top \geq \mathbf{0}_{\mathbb{R}^3}$ *associated with the multi-objective problem* (11) *and* (12) *(see* (21)*), and any observation solutions* $\mathbf{x}^{obs} \in L^2(0,T)^3$*, the adjoint system is defined by the backward linear system*

$$-\mathbf{w}'(t) - [D_{\mathbf{x}}\mathbf{F}(t, \mathbf{x}^*; \mathbf{v}^*)]^\top \mathbf{w}(t) = \alpha_1 \Big(\mathbf{x}^*(t) - \mathbf{x}^{obs}(t)\Big) + \alpha_2 (0,1,0)^\top, \tag{51}$$

$$\mathbf{w}(T) = \mathbf{0}_{\mathbb{R}^3}, \tag{52}$$

admits a unique solution $\mathbf{w}(t)$ *in the Sobolev space* $W^{1,2}([0,T];\mathbb{R}^3)$*.*

Proof. The fact that (51) and (52) defines the adjoint state associated with the multi-objective optimization problem (11) and (12) can be deduced in a standard sense from the scalarized objective function (21). Meanwhile, the well-posedness of this system can be readily deduced by introducing a time-reversal transformation as follows. By applying the time-reversal coordinate transformation $\tau = T - t$, the backward linear system (51) is mapped into a standard forward initial value problem on the compact interval $\tau \in [0,T]$ with homogeneous initial data $\mathbf{w}(0) = \mathbf{0}_{\mathbb{R}^3}$. The transformed system is written as

$$\frac{d\mathbf{w}}{d\tau} = -[D_{\mathbf{x}}\mathbf{F}]^\top \mathbf{w} + \alpha_1 \Big(\mathbf{x}^*(t) - \mathbf{x}^{\text{obs}}(t)\Big) + \alpha_2 (0,1,0)^\top.$$

Since the optimal trajectory $\mathbf{x}^*(t)$ is continuous on $[0,T]$, the entries of $D_{\mathbf{x}}\mathbf{F}$ are continuous and bounded. Combined with the condition $\mathbf{v}^*(t) \in \mathcal{U}_{\text{ad}} \subset L^\infty(0,T)^3$, the coefficient matrix satisfies $[D_{\mathbf{x}}\mathbf{F}]^\top \in L^\infty(0,T)^{3\times 3} \subset L^1(0,T)^{3\times 3}$. Furthermore, since $\mathbf{x}^* \in W^{1,2}([0,T];\mathbb{R}^3) \subset L^2(0,T)^3$ and $\mathbf{x}^{\text{obs}} \in L^2(0,T)^3$, the source vector satisfies

$$\alpha_1 \Big(\mathbf{x}^*(t) - \mathbf{x}^{\text{obs}}(t)\Big) + \alpha_2 (0,1,0)^\top \in L^2(0,T)^3 \subset L^1(0,T)^3.$$

Thus, by the classical Carathéodory existence theorem [23], there exists a unique absolutely continuous solution $\mathbf{w}(\tau)$ on $[0,T]$. Isolating the derivative yields $\mathbf{w}'$. Since $\mathbf{w}$ is continuous and bounded on the compact interval, the product satisfies $[D_{\mathbf{x}}\mathbf{F}]^\top \mathbf{w} \in L^\infty(0,T)^3 \subset L^2(0,T)^3$. The linear combination of two L^2 vectors guarantees that $\mathbf{w}' \in L^2([0,T];\mathbb{R}^3)$, which formally completes the proof that $\mathbf{w} \in W^{1,2}([0,T];\mathbb{R}^3)$. □

Furthermore, the constraint qualification (surjectivity of $\mathcal{M}'$) established in Lemma 3 guarantees the regularity of the constraint operator, ensuring that $K_T = \ker(\mathcal{M}'(\mathbf{x}^*, \mathbf{v}^*))$ via Lyusternik's Theorem and providing the unique representation of the co-state vector $\mathbf{w} \in W^{1,2}([0,T];\mathbb{R}^3)$.

Theorem 3. *Assume that the hypotheses of Lemma 1 are satisfied, and consider the Jacobian notation defined in Lemma 2. Let* $\mathbf{v}^* \in \mathcal{U}_{ad}$ *be a weak Pareto-optimal solution to the multi-objective problem* (11) *and* (12)*, and let* $\mathbf{x}^* \in W^{1,2}([0,T];\mathbb{R}^3)$ *be its corresponding unique state trajectory. Then, there exists a vector of non-negative objective multipliers* $\alpha = (\alpha_1, \alpha_2, \alpha_3)^\top$ *that cannot vanish simultaneously (*$\alpha \neq 0$*). Furthermore, the constraint qualification (surjectivity of* $\mathcal{M}'$*) established in Lemma 3 guarantees the regularity of the constraint operator, ensuring the existence of a unique co-state vector* $\mathbf{w} \in W^{1,2}([0,T];\mathbb{R}^3)$ *satisfying the backward linear adjoint system* (51) *and* (52)*. Moreover, the following compact variational inequality holds:*

$$\int_0^T \Big[\alpha_3(0,0,1) - [D_{\mathbf{v}}\mathbf{F}(t, \mathbf{x}^*; \mathbf{v}^*)]^\top \mathbf{w}(t)\Big]^\top (\tilde{\mathbf{v}}(t) - \mathbf{v}^*(t))\, dt \geq 0, \tag{53}$$

for all alternative admissible design configurations $\tilde{\mathbf{v}} \in \mathcal{U}_{ad}$*.*

Proof. Since $(\mathbf{x}^*, \mathbf{v}^*)$ is a weak Pareto-optimal solution, the intersection of the individual descent cones K_{d_i} and the tangent cone K_T is empty. By the Dubovitskii–Milyutin theorem [13], there exist continuous linear functionals $f_i \in K_{d_i}^*$ and $f_T \in K_T^*$, not all identically zero, satisfying the abstract Euler–Lagrange equation:

$$f_1 + f_2 + f_3 + f_T = 0_{E^*}. \tag{54}$$

From Lemma 1, the descent functionals are characterized by $f_i = -\alpha_i J_i'(\mathbf{x}^*, \mathbf{v}^*)$ for non-negative multipliers $\alpha_i \geq 0$. We claim that the multiplier vector $\alpha = (\alpha_1, \alpha_2, \alpha_3)^\top$ cannot vanish identically ($\alpha \neq 0$). Indeed, if we assume by contradiction that $\alpha = 0$, then $f_1 = f_2 = f_3 = 0_{E^*}$. From (54), it follows directly that $f_T = 0_{E^*}$, yielding $f_1 = f_2 = f_3 = f_T = 0_{E^*}$, which contradicts the fundamental assertion of the Dubovitskii–Milyutin theorem that these functionals are not all identically zero.

For any arbitrary direction $(\tilde{\mathbf{x}}, \tilde{\mathbf{v}})^\top \in K_T = \ker(\mathcal{M}'(\mathbf{x}^*, \mathbf{v}^*))$, we have $f_T(\tilde{\mathbf{x}}, \tilde{\mathbf{v}}) = 0$, so evaluating (54) along such tangent directions yields:

$$\alpha_1 \int_0^T (\mathbf{x}^* - \mathbf{x}^{\text{obs}})^\top \tilde{\mathbf{x}}\, dt + \alpha_2 \int_0^T \tilde{x}_2\, dt + \alpha_3 \int_0^T \tilde{v}_3\, dt = 0. \tag{55}$$

By invoking the second canonical basis vector $\mathbf{e}_2 = (0, 1, 0)^\top$ and the third canonical basis vector $\mathbf{e}_3 = (0, 0, 1)^\top$, we notice that $\tilde{x}_2(t) = \mathbf{e}_2^\top \tilde{\mathbf{x}}(t)$ and $\tilde{v}_3(t) = \mathbf{e}_3^\top \tilde{\mathbf{v}}(t)$. Thus, Equation (55) can be rewritten compactly as:

$$\int_0^T \left[\alpha_1 (\mathbf{x}^*(t) - \mathbf{x}^{\text{obs}}(t)) + \alpha_2 \mathbf{e}_2\right]^\top \tilde{\mathbf{x}}(t)\, dt + \int_0^T \alpha_3 \mathbf{e}_3^\top \tilde{\mathbf{v}}(t)\, dt = 0. \tag{56}$$

From Lemma 4, any element belonging to the tangent cone satisfies the linearized relation $\tilde{\mathbf{x}}' - D_{\mathbf{x}}\mathbf{F}\tilde{\mathbf{x}} - D_{\mathbf{v}}\mathbf{F}\tilde{\mathbf{v}} = \mathbf{0}_{L^2}$ with $\tilde{\mathbf{x}}(0) = \mathbf{0}_{\mathbb{R}^3}$. We test the adjoint differential equation (51) by taking the inner product with the state perturbation vector $\tilde{\mathbf{x}}(t)$ and integrating over the time domain $[0, T]$:

$$\begin{aligned} &\int_0^T \Big(-\mathbf{w}(t)' - [D_{\mathbf{x}}\mathbf{F}(t, \mathbf{x}^*; \mathbf{v}^*)]^\top \mathbf{w}(t) \Big)^\top \tilde{\mathbf{x}}(t)\, dt \\ &\qquad = \int_0^T \Big[\alpha_1 \big(\mathbf{x}^*(t) - \mathbf{x}^{\text{obs}}(t)\big) + \alpha_2 \mathbf{e}_2\Big]^\top \tilde{\mathbf{x}}(t)\, dt. \end{aligned} \tag{57}$$

Applying integration by parts to the first term on the left-hand side, we obtain explicitly $-\int_0^T \langle \mathbf{w}'(t), \tilde{\mathbf{x}}(t) \rangle\, dt = \mathbf{w}(0)^\top \tilde{\mathbf{x}}(0) - \mathbf{w}(T)^\top \tilde{\mathbf{x}}(T) + \int_0^T \langle \mathbf{w}(t), \tilde{\mathbf{x}}'(t) \rangle\, dt$. By invoking the homogeneous initial condition of the linearized state ($\tilde{\mathbf{x}}(0) = \mathbf{0}_{\mathbb{R}^3}$) along with the zero terminal co-state condition ($\mathbf{w}(T) = \mathbf{0}_{\mathbb{R}^3}$), the boundary terms vanish identically, transferring the weak derivative operator cleanly as $-\int_0^T (\mathbf{w}')^\top \tilde{\mathbf{x}}\, dt = \int_0^T \mathbf{w}^\top \tilde{\mathbf{x}}'\, dt$. Regrouping the transpose matrix products in (57) successfully yields the consistent pairing:

$$\int_0^T \mathbf{w}^\top \big(\tilde{\mathbf{x}}' - D_{\mathbf{x}}\mathbf{F}\tilde{\mathbf{x}}\big)\, dt = \int_0^T \left[\alpha_1 (\mathbf{x}^* - \mathbf{x}^{\text{obs}}) + \alpha_2 \mathbf{e}_2\right]^\top \tilde{\mathbf{x}}\, dt. \tag{58}$$

Substituting the dynamic relation of the linearized kernel constraint ($\tilde{\mathbf{x}}' - D_{\mathbf{x}}\mathbf{F}\tilde{\mathbf{x}} = D_{\mathbf{v}}\mathbf{F}\tilde{\mathbf{v}}$) into Equation (58) recovers the following core duality cancellation identity with absolute sign and matrix-transpose consistency:

$$\begin{aligned} \int_0^T \mathbf{w}^\top (D_{\mathbf{v}}\mathbf{F}\tilde{\mathbf{v}})\, dt &= \int_0^T \Big([D_{\mathbf{v}}\mathbf{F}]^\top \mathbf{w}\Big)^\top \tilde{\mathbf{v}}\, dt \\ &= \int_0^T \left[\alpha_1 (\mathbf{x}^* - \mathbf{x}^{\text{obs}}) + \alpha_2 \mathbf{e}_2\right]^\top \tilde{\mathbf{x}}\, dt. \end{aligned} \tag{59}$$

Now, replacing the state integral term from the left-hand side of (56) with our duality result (59), the abstract optimality condition isolates strictly in terms of the parameter and control directions:

$$\int_0^T \Big([D_{\mathbf{v}}\mathbf{F}]^\top \mathbf{w}\Big)^\top \tilde{\mathbf{v}}(t)\, dt + \int_0^T \alpha_3 \mathbf{e}_3^\top \tilde{\mathbf{v}}(t)\, dt = 0, \tag{60}$$

which is algebraically equivalent to:

$$\int_0^T \left(\alpha_3 \mathbf{e}_3 + [D_{\mathbf{v}}\mathbf{F}]^\top \mathbf{w}\right)^\top \tilde{\mathbf{v}}(t)\, dt = 0. \tag{61}$$

Finally, since the perturbations represent arbitrary directions pointing inward toward the convex admissible set $\mathcal{U}_{\text{ad}}$ from the optimal strategy, we define the directional parameter–control increment as $\tilde{\mathbf{v}}(t) \to \tilde{\mathbf{v}}(t) - \mathbf{v}^*(t)$. Projecting this difference into the isolated relation (61) transforms the algebraic equality into the definitive continuous variational inequality (53), which completes the proof. □

6. Numerical Approximation and Examples

6.1. Methodological Foundations and Discretization Strategy

In this section, a self-contained optimization framework is developed to numerically approximate the weak Pareto-optimal solutions of the multi-objective optimization problem (11) and (12). Broadly speaking, the forward non-linear compartmental dynamics are resolved utilizing a high-order Runge–Kutta integration scheme, whereas the time-dependent design parameters and control functions are projected onto a finite-dimensional functional subspace that strictly respects the analytical boundaries of the admissible set $\mathcal{U}_{ad}$. Furthermore, to achieve computational scalability under high-dimensional mesh configurations, the resulting continuous-to-discrete optimization flow is driven by an adjoint-based gradient descent method embedded within an Augmented Lagrangian framework, as detailed below.

Before establishing the discrete optimization sequence, a rigorous justification regarding the finite-dimensional projection of the parameter–control tuple $\mathbf{v}(t)$ (see (14)) is mathematically mandatory. While traditional numerical approaches frequently employ global cubic spline interpolations due to their high-order derivative continuity (C^2), such configurations introduce a fundamental theoretical mismatch against the $L^\infty(0,T)$ state regularity proven in Theorem 1, which explicitly permits jump discontinuities to model reactive public health emergency protocols. To resolve this inconsistency, three finite-dimensional approximation regimes over the coarse temporal mesh τ_j were thoroughly evaluated. First, the piecewise constant approximations (C^{-1}) offer absolute theoretical fidelity to the discontinuous structure of L^∞ and inherently eliminate polynomial undershoot, yet severely degrade the local convergence order of the Runge–Kutta state integrator due to step-skipping across sharp boundary horizons. Second, cubic splines with relaxed conditions (C^1) retain high geometric smoothness at the expense of preserving non-physical oscillations between decision nodes, thus requiring artificial clipping safeguards. Third, piecewise linear continuous functions (C^0) form a valid, dense subspace embedded in $L^\infty(0,T)$. From a computational–epidemiological trade-off perspective, the C^0 linear-spline architecture emerges as the optimal choice. It represents realistic operational transitions (i.e., highly steep deterministic policy ramps rather than physically impossible instantaneous shocks), completely avoids mid-interval undershoot to guarantee structural positivity without non-differentiable fine-grid projection operators, and preserves the absolute continuity of the ODE right-hand vector field, thereby ensuring smooth directional derivatives for the numerical optimization solver. Consequently, the piecewise linear framework is adopted hereinafter to construct a self-consistent projection flow.

The resulting finite-dimensional Non-linear Programming (NLP) problem is iteratively resolved by implementing an Augmented Lagrangian Method (ALM) coupled with the exact gradient vectors computed via the backward linear adjoint system (51) and (52). By leveraging the continuous-to-discrete adjoint formulation derived from the geometric Dubovitskii–Milyutin functional formalism, we completely bypass the computationally prohibitive burden of forward finite-difference approximations, reducing the gradient

evaluation cost to just one forward state integration and one backward co-state resolution per optimization iteration. Specifically, the bound constraints defined in $\mathcal{U}_{ad}$ and any generalized non-linear state trajectories are handled by constructing an augmented objective functional. Within each outer iteration of the ALM framework, the resulting unconstrained subproblem is minimized in the reduced parameter space using the exact adjoint-based gradient vector, which is evaluated by projecting the continuous variational characterization (53) onto the piecewise linear continuous subspace. The multiplier vectors and penalty parameters are sequentially updated in the outer loop until the continuous-to-discrete optimality criteria are satisfied, ensuring high stability, scalability for large-scale decision node configurations, and absolute prevention of non-physical numerical oscillations.

6.2. Numerical Discretization Algorithm

To numerically resolve the continuous multi-objective optimization framework formulated in (11) and (12), we implement a finite-dimensional reduction based on the First-Discretize-Then-Optimize approach. This methodology transforms the continuous infinite-dimensional control and parameter spaces into finite-dimensional vector spaces. Driven by an Augmented Lagrangian Method (ALM) and leveraging exact adjoint-based gradients, this mathematical framework completely circumvents the computational burden of forward finite-difference perturbations. To be precise, the continuous-to-discrete optimization flow is structured into five systematic steps detailed below:

Step 1. *Discretization of the domain* $[0, T]$. We partition the time interval $[0, T]$ into two distinct, decoupled temporal grids designed to separate the state trajectory integration from the parameter optimization loop. First, the domain $[0, T]$ is divided into a uniform fine grid of N_t nodes for direct and adjoint state integration, where $t_k = (k-1)\Delta t$ with a fine time-step size $\Delta t = T/(N_t - 1)$ for $k \in \{1, \dots, N_t\}$. Second, we independently construct a uniform coarse parameter mesh over M master control nodes ($M \ll N_t$) defined by $\tau_j = (j-1)\Delta\tau$ with a coarse step size $\Delta\tau = T/(M-1)$, which yields the partition $0 = \tau_1 < \tau_2 < \cdots < \tau_M = T$. This coarse discretization is designed strictly to define the decision variables for the time-dependent parameter and control functions.

Step 2. *Processing of experimental data.* We consider that the experimental clinical observations are originally recorded on a discrete temporal partition $0 = t_1^{\text{obs}} < t_2^{\text{obs}} < \cdots < t_{\overline{M}}^{\text{obs}} = T$. To evaluate the objective tracking functional over the fine integration grid t_k, we construct the continuous-time baseline observation functions $\mathbf{x}_k^{\text{obs}}$ via cubic spline interpolation of the raw discrete data points $\mathbf{x}^{\text{obs}}(t_j^{\text{obs}})$.

Step 3. *Discretization of parameter and control functions.* To establish a rigorous finite-dimensional projection that preserves the continuous topological structure established in Section 6.1, the infinite-dimensional time-dependent parameters $\beta(t)$, $\gamma(t)$, and the vaccination control $u(t)$ are restricted to a finite-dimensional subspace of piecewise linear continuous functions (C^0). Let $\{\phi_j(t)\}_{j=1}^M$ denote the unique set of global linear interpolating basis functions (commonly referred to as hat functions) satisfying the Kronecker delta property $\phi_j(\tau_i) = \delta_{ji}$ over the coarse partition nodes. Consequently, the parameterized approximations are defined globally for $t \in [0, T]$ as follows:

$$\beta_{\Delta\tau}(t) = \sum_{j=1}^{M} \beta_j \phi_j(t), \quad \gamma_{\Delta\tau}(t) = \sum_{j=1}^{M} \gamma_j \phi_j(t), \quad u_{\Delta\tau}(t) = \sum_{j=1}^{M} u_j \phi_j(t), \tag{62}$$

where β_j, γ_j, and u_j represent the explicit nodal decision values at the master temporal coordinate τ_j. Locally, for any subinterval $t \in [\tau_j, \tau_{j+1}]$, these expansions collapse to standard linear segments uniquely determined by their boundary mas-

ter nodes, thereby avoiding polynomial overshooting and naturally guaranteeing monotonicity between nodes. Hence, the complete finite-dimensional decision vector $\mathbf{V} \in \mathbb{R}^{3M}$ for the reduced parameter–control problem is defined by:

$$\mathbf{V} = [\beta_1, \dots, \beta_M, \gamma_1, \dots, \gamma_M, u_1, \dots, u_M]^\top. \tag{63}$$

These nodal configurations are restricted directly by the physical box boundaries prescribed in the admissible set $\mathcal{U}_{ad}$, satisfying $\beta_{\min} \le \beta_j \le \beta_{\max}$, $\gamma_{\min} \le \gamma_j \le \gamma_{\max}$, and $0 \le u_j \le u_{\max}$ for all $j \in \{1, \dots, M\}$.

Step 4. *Approximate solution of the direct and adjoint state systems.* Let us define the parameterized vector field associated with the direct ODE system on the fine grid nodes t_k as:

$$\begin{aligned}\mathbf{F}_{\Delta\tau}(t, \mathbf{x}; \mathbf{V}) = \Big(& -\beta_{\Delta\tau}(t; \mathbf{V}) f(x_1, x_2) - u_{\Delta\tau}(t; \mathbf{V}) g(x_1), \\ & p\beta_{\Delta\tau}(t; \mathbf{V}) f(x_1, x_2) - \gamma_{\Delta\tau}(t; \mathbf{V}) x_2, \\ & u_{\Delta\tau}(t; \mathbf{V}) g(x_1) + (1-p)\beta_{\Delta\tau}(t; \mathbf{V}) f(x_1, x_2) + \gamma_{\Delta\tau}(t; \mathbf{V}) x_2 \Big)^\top.\end{aligned}$$

The unique weak continuous state trajectory (17) is approximated by integrating the forward Cauchy problem:

$$\frac{d\mathbf{x}}{dt} = \mathbf{F}_{\Delta\tau}(t, \mathbf{x}; \mathbf{V}), \quad \mathbf{x}(0) = \mathbf{x}_0, \tag{64}$$

utilizing a high-order Runge–Kutta scheme evaluated over the uniform fine mesh t_k. This procedure yields the discrete state sequence $\mathbf{x}_k = (S_k, I_k, R_k)^\top$ for $k \in \{1, \dots, N_t\}$. Crucially, immediately following the direct solution, the discrete co-state trajectories $\mathbf{w}_k = (w_{1,k}, w_{2,k}, w_{3,k})^\top$ are computed by backward-in-time integration of the linear adjoint system (51) and (52) from t_{N_t} down to t_1, driven by the saved states $\mathbf{x}_k$.

Step 5. *Augmented Lagrangian formulation and exact gradient evaluation.* The integral cost functionals J_1, J_2, and J_3 defined in (7) and (8) are evaluated over the uniform fine integration mesh via the composite trapezoidal rule, providing the discrete sub-objectives:

$$J_{1,\Delta t}(\mathbf{V}) = \frac{\Delta t}{4} \sum_{k=1}^{N_t - 1} \left(\|\mathbf{x}_k - \mathbf{x}_k^{\text{obs}}\|^2 + \|\mathbf{x}_{k+1} - \mathbf{x}_{k+1}^{\text{obs}}\|^2 \right), \tag{65}$$

$$J_{2,\Delta t}(\mathbf{V}) = \frac{\Delta t}{2} \sum_{k=1}^{N_t - 1} (I_k + I_{k+1}), \tag{66}$$

$$J_{3,\Delta t}(\mathbf{V}) = \frac{\Delta t}{2} \sum_{k=1}^{N_t - 1} (u_{\Delta\tau}(t_k) + u_{\Delta\tau}(t_{k+1})), \tag{67}$$

where the continuous-to-discrete scalarized objective functional is given by $\mathcal{J}_{\alpha,\Delta t}(\mathbf{V}) = \sum_{i=1}^{3} \alpha_i J_{i,\Delta t}(\mathbf{V})$. To handle boundary and state-dependent trajectories, we assemble the finite-dimensional Augmented Lagrangian functional $\mathcal{L}_A$ at the n-th iteration as:

$$\mathcal{L}_A(\mathbf{V}, \boldsymbol{\mu}^{(n)}, \rho^{(n)}) = \mathcal{J}_{\alpha,\Delta t}(\mathbf{V}) + \mathcal{P}(\mathbf{V}, \boldsymbol{\mu}^{(n)}, \rho^{(n)}) + \lambda \mathcal{R}_{\text{Tikh}}(\mathbf{V}), \tag{68}$$

where $\boldsymbol{\mu}^{(n)}$ represents the vector of Lagrange multipliers, $\rho^{(n)} > 0$ is the penalty parameter, and $\mathcal{R}_{\text{Tikh}}(\mathbf{V})$ is the first-order Tikhonov regularizer mapping the L^2-norm of the parameter derivatives over the coarse nodes:

$$\mathcal{R}_{\text{Tikh}}(\mathbf{V}) = \sum_{j=1}^{M-1} \left[(\beta_{j+1} - \beta_j)^2 + (\gamma_{j+1} - \gamma_j)^2 + (u_{j+1} - u_j)^2 \right]. \tag{69}$$

The exact gradient $\nabla_{\mathbf{V}}\mathcal{L}_A$ is calculated algebraically in each iteration by projecting the continuous necessary optimality condition (53) using the coupled values of the forward state $\mathbf{x}_k$ and backward co-state $\mathbf{w}_k$, completely eliminating forward finite-difference numerical perturbations.

The resulting finite-dimensional Non-linear Programming (NLP) problem is solved iteratively by minimizing the unconstrained subproblem within the Augmented Lagrangian loop using a low-memory quasi-Newton optimization algorithm with bound support, such as L-BFGS-B, as illustrated in the updated flowchart of Figure 2. Within this modern iterative framework, the exact gradients of the augmented objective function with respect to the nodal decision parameters $\mathbf{V}$ are evaluated algebraically by invoking the continuous-to-discrete adjoint mapping. This implementation reduces the optimization computational complexity significantly, as it requires only a single forward direct integration and one backward co-state integration per iteration.

Regarding the algorithmic implementation, the inclusion of the first-order Tikhonov regularization term defined in (69) into the Augmented Lagrangian structure (68) addresses the well-known ill-posedness inherent to simultaneous parameter identification and optimal control inverse problems. In the continuous-time domain, this formulation maps directly to a first-order derivative derivative penalty:

$$\mathcal{J}_{\text{reg}}(\mathbf{v}) = \mathcal{J}_{\alpha}(\mathbf{v}) + \lambda \int_0^T \left| \frac{d\mathbf{v}}{dt} \right|^2 dt, \tag{70}$$

where $\lambda > 0$ is a positive regularization parameter designed to suppress high-frequency physical oscillations and bound the total variation in the reconstructed functions. In our discrete representation, this penalty effectively restricts large structural jumps between adjacent master nodes on the coarse optimization grid τ_j.

Crucially, the adoption of the piecewise linear continuous C^0 functional framework inherently resolves the primary computational challenge associated with traditional high-order cubic interpolations. While cubic expansions frequently suffer from non-physical polynomial undershoot phenomena between adjacent decision nodes (forcing the deployment of non-differentiable fine-grid clipping operators such as $\max(0, \cdot)$), the linear-spline architecture satisfies local monotonicity properties. Because the box constraints from the admissible set $\mathcal{U}_{ad}$ are rigorously and explicitly enforced at each master coordinate τ_j by the bound-constrained solver, the continuous parameters $\beta_{\Delta\tau}(t)$, $\gamma_{\Delta\tau}(t)$, and $u_{\Delta\tau}(t)$ are mathematically guaranteed to remain strictly bounded and non-negative throughout the entire continuous-time horizon $[0, T]$. Consequently, the epidemic vector field and the augmented systemic costs are evaluated exclusively over epidemiologically meaningful, smooth, and fully differentiable trajectories without requiring artificial numerical safeguards.

6.3. Example 1: The Classic 1978 Boarding School Influenza Outbreak Under Standard Bilinear Transmission

In this example, we evaluate the performance of the proposed identification framework utilizing the experimental data from the classic 1978 boarding school influenza outbreak [25]. It is well established by international consensus that the standard deterministic validation of the SIR model (3)–(6) under a bilinear incidence force $f(s, i) = si$, subclinical immunity $p = 1$, and a fixed closed population size $N = 763$, yields a constant transmission rate $\beta \approx 1.66$ days^{-1} and a constant recovery rate $\gamma \approx 0.44$ days^{-1}, which corresponds to an average infectious period of $\gamma^{-1} \approx 2.27$ days. This classical, uniform parameterization and its trajectory-matching criteria are widely documented across epidemiological optimization frameworks [26]. In the present study, this classical framework is significantly generalized to encompass time-dependent functions $\beta(t)$ and $\gamma(t)$ reconstructed within the

piecewise linear continuous C^0 functional subspace. Crucially, the simultaneous parameter reconstruction and optimal vaccination scheduling are driven by the exact adjoint-based gradient descent embedded within the Augmented Lagrangian Method (ALM) framework, ensuring robust enforcement of the physical and dynamic constraints without numerical finite-difference perturbations.

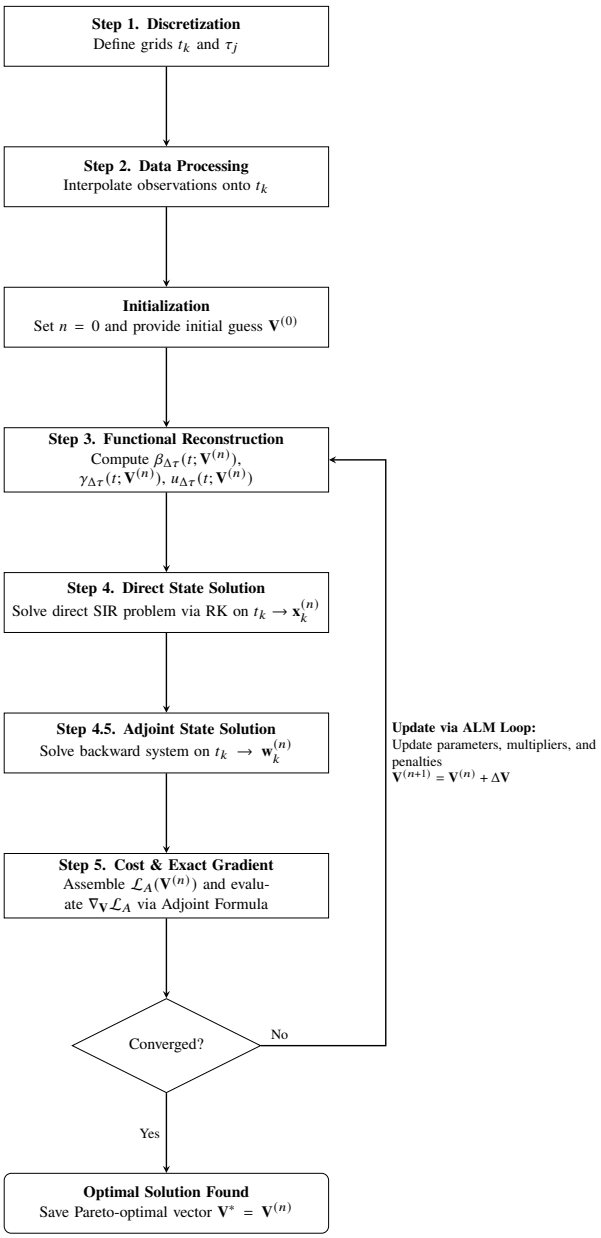

Figure 2. Iterative flowchart of the First-Discretize-Then-Optimize scheme featuring the Augmented Lagrangian Method (ALM) optimization loop and exact adjoint gradient evaluations.

The multi-objective optimization results for the classic 1978 boarding school influenza outbreak, resolved via the exact adjoint-based Augmented Lagrangian Method (ALM), are schematically illustrated in Figure 3. The algorithm was initialized with the uniform initial guesses $\beta_j = 0.0022$, $\gamma_j = 0.4400$, and $u_j = 0.0100$ for all $j \in \{1, \dots, M\}$, over a fine temporal grid of $N_t = 1000$ integration nodes and a coarse parameter mesh of $M = 13$ master nodes. The scalarization preferences and the first-order Tikhonov regularization parameter were set to $\boldsymbol{\alpha} = (0.8, 0.1, 0.1)$ and $\lambda = 10^{-4}$, respectively. Figure 3a–c display the optimal state trajectories computed on the fine grid t_k, superimposed onto the historical medical

bed-confinement measurements compiled in Table 1. The reconstructed state solutions for the susceptible $S(t)$, infectious $I(t)$, and recovered $R(t)$ populations exhibit an exceptional tracking performance, successfully dampening observational noise without high-frequency overfitting. The continuous-to-discrete framework accurately captures the critical epidemiological phases of the outbreak, including the rapid depletion of susceptibles, the sharp escalation toward the infectious peak around day 6, and the subsequent stabilization during the disease remission phase.

Table 1. Experimental time series of the 1978 influenza outbreak in a British boarding school ($N = 763$), deduced from the medical bed-confinement records [25].

t (Days)	$S(t)$	$I(t)$	$R(t)$
0	762	1	0
1	760	3	0
2	757	6	0
3	738	25	0
4	689	73	1
5	535	222	6
6	444	294	25
7	432	258	73
8	304	237	222
9	175	191	397
10	143	125	495
11	141	69	553
12	141	27	595
13	141	11	611
14	141	4	618

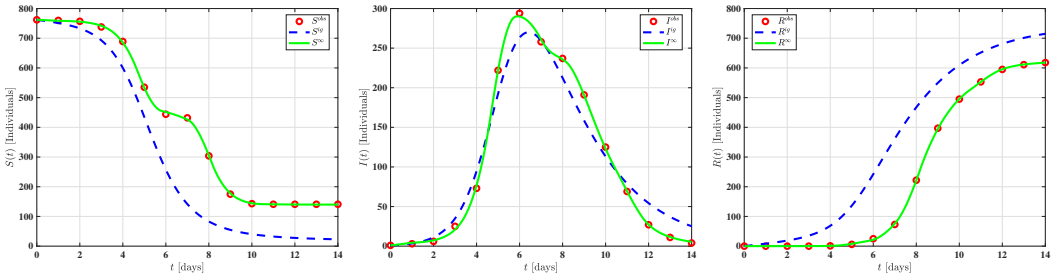

(**a**) Susceptible population (**b**) Infected population (**c**) Recovered population

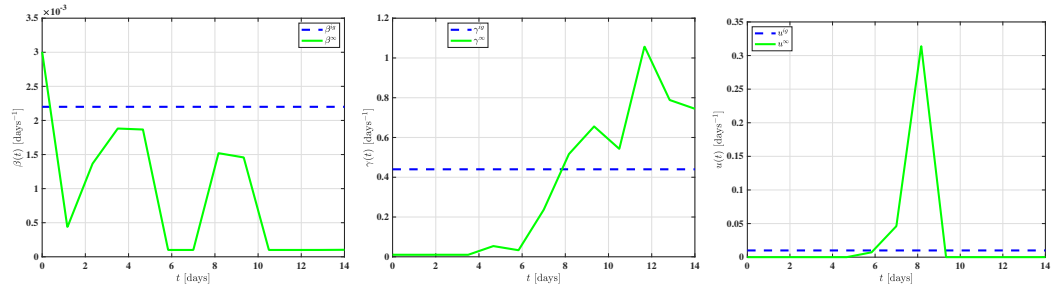

(**d**) Transmission rate (**e**) Recovery rate (**f**) Vaccination control

Figure 3. Multi-objective results for the 1978 influenza on Example 1. (**a**–**c**) display the state solutions fitted to experimental data. (**d**–**f**) illustrate the regularized time-dependent functions β, γ and u. See Table 2 for numerical values of the coefficients for $\beta_{\Delta t}$, $\gamma_{\Delta t}$ and $u_{\Delta t}$.

Table 2. Optimal master nodes and temporal grid configurations τ_j for the time-dependent functions $\beta(t)$, $\gamma(t)$, and $u(t)$ obtained via the exact adjoint-based Augmented Lagrangian Method (ALM) loop ($M = 13$).

j	τ_j	β_j	γ_j	u_j
1	0.0000	3.0048×10^{-3}	1.0190×10^{-2}	1.5385×10^{-6}
2	1.1667	4.3249×10^{-4}	1.0051×10^{-2}	1.0426×10^{-6}
3	2.3333	1.3658×10^{-3}	1.0165×10^{-2}	4.7971×10^{-6}
4	3.5000	1.8814×10^{-3}	1.0016×10^{-2}	1.0885×10^{-6}
5	4.6667	1.8670×10^{-3}	5.3831×10^{-2}	2.0086×10^{-5}
6	5.8333	1.0009×10^{-4}	3.3030×10^{-2}	7.1968×10^{-3}
7	7.0000	1.0010×10^{-4}	2.3666×10^{-1}	4.6215×10^{-2}
8	8.1667	1.5200×10^{-3}	5.1660×10^{-1}	3.1478×10^{-1}
9	9.3333	1.4574×10^{-3}	6.5554×10^{-1}	2.1201×10^{-5}
10	10.5000	1.0002×10^{-4}	5.4263×10^{-1}	1.8964×10^{-6}
11	11.6667	1.0005×10^{-4}	1.0582×10^{0}	2.1178×10^{-6}
12	12.8333	1.0022×10^{-4}	7.8853×10^{-1}	3.5661×10^{-6}
13	14.0000	1.0250×10^{-4}	7.4448×10^{-1}	2.0347×10^{-5}

Figure 3d–f depict the optimal time-dependent functions $\beta(t)$, $\gamma(t)$, and the vaccination control strategy $u(t)$ reconstructed within the piecewise linear continuous C^0 functional subspace. Driven by the exact gradient projections and the first-order Tikhonov penalty, the estimated functions remain strictly bounded within the admissible region $\mathcal{U}_{ad}$ throughout the entire time horizon $[0, T]$, ensuring structural biological validity without requiring non-differentiable fine-grid clipping operators. Specifically, the transmission rate $\beta(t)$ in panel (d) captures the dynamic, non-constant nature of the contact pathways, dropping to its operational lower bound of 1.0009×10^{-4} during the accelerated phase (day 6) as a consequence of public health awareness and behavioral feedback, before recovering slightly. Concurrently, the recovery rate $\gamma(t)$ in panel (e) stays strictly bounded above its physical lower limit $\gamma_{\min} = 10^{-2}$, adjusting dynamically between 1.0051×10^{-2} and 1.0582×10^{0} to reflect the non-uniform patient remission and confinement rates.

Finally, panel (f) illustrates the optimal scheduling of the reactive mitigation control policy $u(t)$. In contrast to smooth polynomial interpolations, the adopted piecewise linear continuous architecture satisfies strict local monotonicity properties, naturally preventing non-physical undershoot oscillations. The resulting intervention profile exhibits a highly responsive, sharp peak concentrated between days 6 and 9, achieving its maximum public health operational intensity of $u_8 = 3.1478 \times 10^{-1}$ days^{-1} at the master control node $\tau_8 = 8.1667$ days. This localized, wedge-shaped distribution precisely matches the period of maximum infectious prevalence, demonstrating how the optimal allocation of emergency countermeasures reactively counteracts the transmission acceleration while concurrently minimizing the joint scalarized expenditure of disease prevalence ($J_{2,\Delta t}$) and public health structural implementation costs ($J_{3,\Delta t}$).

Consequently, this implementation serves a dual methodological and epidemiological benchmark purpose. Rather than simply fitting data, this configuration evaluates a retrospective "what-if" public health scenario, assessing how the synthesis of non-dominated, reactive emergency policies dynamically shapes epidemic containment when competing directly against administrative expenditures and historical infection waves. This baseline confirms that the exact adjoint-based Augmented Lagrangian algorithm operates as a highly robust computational engine, ensuring that public health decision-makers can reliably filter operational noise, identify underlying time-dependent transmission rates ($\beta(t)$ and $\gamma(t)$), and design optimal, proactive response mechanisms even when dealing with historical data or newly emerging pathogens lacking prior recorded control interventions.

Regarding the structural properties of the estimated time-dependent trajectories, the qualitative behaviors of $\beta(t)$, $\gamma(t)$, and $u(t)$ are strictly governed by the underlying functional analytical framework established in Section 2. Rather than imposing artificial high-order smoothness through traditional global splines, the adoption of the piecewise linear continuous C^0 architecture balances geometric flexibility with numerical stability. The macroscopic smoothness and the prevention of high-frequency physical oscillations are mathematically controlled by the first-order Tikhonov regularization penalty, which maps directly to the minimization of the L^2-norm of the weak derivatives in the continuous-time domain (70). Consequently, the parameters exhibit fluid, stable interval-by-interval transitions that preserve the continuous topological properties proved in Theorem 1. This formulation remains fully consistent with the $L^\infty(0,T)$ regularity condition prescribed in the admissible set $\mathcal{U}_{ad}$, confirming that the multi-objective algorithm accurately reconstructs parameterized dynamics that are robust, physically bounded, and rigorously aligned with the Carathéodory weak solution framework.

6.4. Example 2: The 2009 Pandemic Influenza A (H1N1) Outbreak with Behavioral Saturation

In this example, we evaluate the capabilities of the proposed continuous-to-discrete optimization framework under non-linear saturation transmission forces. We construct a synthetic benchmark scenario inspired by the epidemiological parameters reported by Chowell et al. [27] for the 2009 pandemic influenza A (H1N1) outbreak in San Luis Potosí, Mexico. During this specific epidemic wave, public awareness, widespread protective facemask adoption, and reactive social distancing induced a notable behavioral reduction in effective contact rates prior to official institutional interventions. To model this dynamic behavioral feedback mathematically, we activate the Behncke-type non-linear transmission force formulated in (1) by setting $f(s,i) = si/(1+\bar{\alpha}s)$, where $\bar{\alpha} = 0.005$ denotes the behavioral saturation coefficient penalizing high-density contact configurations due to societal panic. Moreover, we prescribe subclinical immunity $p = 1$ and a state-dependent removal rate $g(s) = s$.

The synthetic experimental dataset is generated by computing the ground-truth forward trajectories of the state system (3)–(6) over a temporal horizon of $T = 11$ days under a constant baseline transmission rate $\beta = 0.0084$ days^{-1}, a constant recovery rate $\gamma = 0.1650$ days^{-1}, and $u(t) = 0$, subjected to the exact initial conditions $(s_0, i_0, r_0) = (209, 1, 0)$ for a total closed population of $N = 210$. The synthetic time series, explicitly detailed in Table 3, is obtained by daily sampling of the continuous forward integration, which is subsequently rounded to the nearest integer. This deterministic quantization, rather than the injection of stochastic noise, is intentionally introduced to replicate the discrete count nature of public health records. The resulting non-smooth integer sequence serves as the tracking observation trajectory $\mathbf{x}^{\text{obs}}$ within the multi-objective cost functional, thereby rigorously testing the capability of the exact adjoint-based Augmented Lagrangian Method (ALM) to handle quantization errors without losing structural identifiability under a piecewise linear C^0 representation.

The numerical tracking performance and the regularized parameter profiles for the 2009 H1N1 influenza outbreak with behavioral saturation are depicted in Figure 4. To achieve high computational fidelity within the multi-objective optimization loop, the state trajectories were integrated across a highly refined discrete grid containing $N_t = 1000$ nodes. The algorithm was initialized with the uniform initial guesses $\beta_j = 0.005$, $\gamma_j = 0.0300$, and $u_j = 0.0100$ for all $j \in \{1, \dots, M\}$, over a coarse optimization partition of $M = 9$ master nodes. For the composite cost functional, we prescribed the scalarization weight vector $\boldsymbol{\alpha} = (0.8, 0.1, 0.1)$ and a first-order Tikhonov regularization parameter $\lambda = 10^{-4}$.

Table 3. Synthetic experimental time series generated via forward simulation of the state equations under constant parameters for Example 2 ($\beta = 0.0084$ days^{-1}, $\gamma = 0.1650$ days^{-1}, $N = 210$, $\overline{\alpha} = 0.005$, $u = 0, p = 1$).

t (Days)	$S(t)$	$I(t)$	$R(t)$
0	209	1	0
1	208	2	0
2	205	4	1
3	200	8	2
4	191	15	4
5	174	29	7
6	144	52	14
7	102	84	24
8	56	113	41
9	24	125	61
10	9	120	81
11	4	106	100

As shown in Figure 4a–c, the exact adjoint-based Augmented Lagrangian Method (ALM) successfully filters the deterministic epidemic structure from the quantized integer dataset, yielding smooth, biologically consistent state trajectories for $S(t)$, $I(t)$, and $R(t)$ that completely avoid high-frequency numerical overfitting. Driven by the dampening effects of the Behncke-type non-linear behavioral saturation force, the infectious curve is tightly regulated, successfully stabilizing the tracking error across the entire observation horizon despite the non-smooth quantization present in the empirical time series.

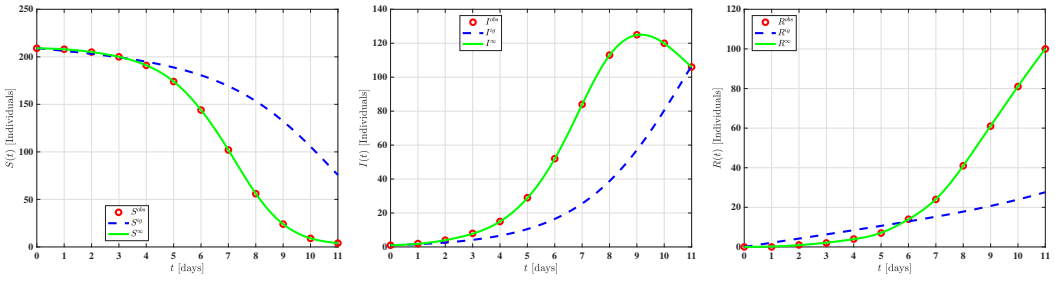

(**a**) Susceptible population (**b**) Infected population (**c**) Recovered population

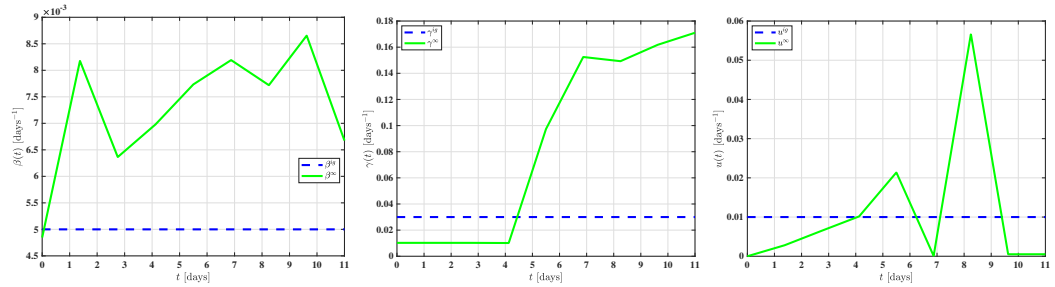

(**d**) Transmission rate (**e**) Recovery rate (**f**) Vaccination control

Figure 4. Multi-objective results for the influenza A (H1N1) with saturation given on Example 2. (**a**–**c**) display the state solutions fitted to experimental data. (**d**–**f**) illustrate the regularized time-dependent functions β, γ and u. See Table 4 for numerical values of the coefficients for $\beta_{\Delta t}$, $\gamma_{\Delta t}$ and $u_{\Delta t}$.

Table 4. Optimal master nodes and temporal grid configurations τ_j for the time-dependent functions $\beta(t)$, $\gamma(t)$, and $u(t)$ obtained via the exact adjoint-based Augmented Lagrangian Method (ALM) loop ($M = 9$).

j	τ_j (Days)	β_j	γ_j	u_j
1	0.0000	4.8456×10^{-3}	1.0255×10^{-2}	1.9996×10^{-6}
2	1.3750	8.1782×10^{-3}	1.0260×10^{-2}	2.8070×10^{-3}
3	2.7500	6.3641×10^{-3}	1.0251×10^{-2}	6.5175×10^{-3}
4	4.1250	6.9800×10^{-3}	1.0131×10^{-2}	1.0167×10^{-2}
5	5.5000	7.7337×10^{-3}	9.7329×10^{-2}	2.1379×10^{-2}
6	6.8750	8.1928×10^{-3}	1.5248×10^{-1}	8.6285×10^{-5}
7	8.2500	7.7194×10^{-3}	1.4927×10^{-1}	5.6689×10^{-2}
8	9.6250	8.6546×10^{-3}	1.6182×10^{-1}	5.0713×10^{-4}
9	11.0000	6.6746×10^{-3}	1.7104×10^{-1}	5.1477×10^{-4}

The accompanying parametric mechanisms that govern this optimized dynamic are further clarified in Figure 4d–f. Rather than maintaining a rigid, artificially uniform value, the reconstructed transmission rate $\beta(t)$ and the recovery rate $\gamma(t)$ adapt fluidly interval by interval across the C^0 linear continuous interpolation domain. The macroscopic smoothness of these transitions is rigorously guaranteed by the spatial penalty term, which preserves topological continuity without requiring non-differentiable fine-grid clipping safeguards.

In parallel, the optimal reactive mitigation control strategy $u(t)$ operates dynamically to minimize the joint epidemiological burden. The policy remains effectively latent during the early acceleration phases ($t < 4$ days), satisfying the local monotonicity properties inherent to the linear spline architecture. As infected cases accumulate, the control undergoes a targeted, highly responsive escalation, achieving its peak public health intervention intensity of $u_7 = 5.6689 \times 10^{-2}$ days^{-1} at the master control node $\tau_7 = 8.2500$ days, before dropping sharply as the outbreak transitions into its remission phase. This coordinated numerical profiling directly preserves mathematical consistency with the exact nodal coordinates compiled in Table 4, providing a robust and fully differentiable inverse estimation framework.

Remark 2. *Regarding the numerical values compiled in Table 4, a noteworthy structural transition is observed in the recovery rate $\gamma(t)$, which undergoes a steep increase from $\tau_4 = 4.125$ days ($\gamma_4 \approx 1.01 \times 10^{-2}$) to $\tau_5 = 5.500$ days ($\gamma_5 \approx 9.73 \times 10^{-2}$). This localized acceleration is fully driven by the empirical trajectory adjustments required to capture the explosive growth phase of the infectious class $I(t)$ documented in Table 3 between days 4 and 7. Crucially, this steep ramp is fully compliant with the continuous C^0 functional framework proven in Theorem 1. Piecewise linear expansions inherently accommodate high-magnitude directional slopes between adjacent master decision nodes without requiring continuous derivatives (C^1 or C^2), providing the algorithm with the exact geometric flexibility needed to filter structural transitions without inducing non-physical numerical undershoot.*

6.5. Example 3: Pareto Sensitivity

To rigorously assess the structural robustness of the identification framework, a Pareto sensitivity analysis is conducted to evaluate the influence of the multi-objective scalarization weights on the simultaneous reconstruction of the time-dependent functions $\beta_{\Delta\tau}(t)$, $\gamma_{\Delta\tau}(t)$, and $u_{\Delta\tau}(t)$. Instead of examining an arbitrary continuum of the Pareto front, we systematically explore three distinct scalarization scenarios designed to contrast competing epidemiological, computational, and economic priorities.

From the numerical results illustrated in Figure 5, we observe three distinct operational regimes that govern the Pareto efficient frontier. First, when a heavy tracking profile is enforced by setting $\alpha = [0.8, 0.1, 0.1]$, the optimization routine prioritizes the minimization

of the empirical data deviations $J_{1,\Delta t}$, yielding reconstructed state trajectories for the susceptible $S(t)$ and infectious $I(t)$ populations that match the discrete quantized historical data points with high precision. However, this excellent tracking performance is achieved at the expense of a weak epidemiological intervention, allowing a higher cumulative infectious burden due to the low priority assigned to $J_{2,\Delta t}$. Conversely, when the public health priority dominates the optimization objective through the second scenario, $\alpha = [0.1, 0.8, 0.1]$, a radical flattening of the epidemic curve is achieved because the algorithm forces the optimal vaccination control strategy $u(t)$ to undergo an aggressive and early escalation; this intense immunizing barrier significantly dampens the transmission mechanism, but it introduces a visible misalignment with respect to the baseline quantized data points, thereby illustrating the competing nature of the inverse formulation. Finally, under the third scenario, $\alpha = [0.1, 0.1, 0.8]$, the control energy $J_{3,\Delta t}$ is heavily penalized, and the resulting optimized control profile suppresses aggressive or prolonged vaccination campaigns to prevent high public health expenditures, yielding intermediate epidemic curves that represent the most economically viable strategy on the non-dominated front. This simultaneous mapping verifies the capability of the first-discretize-then-optimize routine to isolate transparent decision-making regions.

To rigorously assess the structural robustness and identifiability of the proposed optimization framework, a Pareto sensitivity analysis is conducted by evaluating the influence of the multi-objective scalarization weights on the simultaneous reconstruction of the time-dependent functions $\beta_{\Delta\tau}(t)$, $\gamma_{\Delta\tau}(t)$, and $u_{\Delta\tau}(t)$. Instead of examining an arbitrary continuum of the Pareto front, we systematically explore three distinct scalarization scenarios designed to contrast competing epidemiological, computational, and economic priorities across both previous outbreak contexts. The first scenario, configured with $\alpha = [0.8, 0.1, 0.1]$, assigns heavy priority to the data-tracking functional $J_{1,\Delta t}$, forcing the algorithm to strictly match the clinical history. The second scenario, defined by $\alpha = [0.1, 0.8, 0.1]$, prioritizes the public health objective $J_{2,\Delta t}$ to achieve a radical minimization of the total infectious burden. Finally, the third scenario utilizes a heavy weight configuration $\alpha = [0.1, 0.1, 0.8]$ to emphasize the optimization of the control energy $J_{3,\Delta t}$, thereby penalizing aggressive vaccination policies to identify the most economically viable intervention profile. The numerical trajectories and reconstructed coefficients are illustrated in Figure 5, where panels (a) and (b) correspond to the configurations of Section 6.3 and Section 6.4, respectively.

The numerical results computed via the adjoint-based Augmented Lagrangian Method (ALM) reveal three distinct operational regimes that govern the non-dominated Pareto efficient frontier. As shown in the top rows of Figure 5a,b, when the heavy data-tracking profile ($\alpha = [0.8, 0.1, 0.1]$) is enforced, the optimization routine successfully prioritizes the minimization of empirical deviations, yielding state trajectories for the susceptible $S(t)$, infectious $I(t)$, and recovered $R(t)$ populations that trace the historical data points with high precision. However, this tight fit is achieved at the expense of a relaxed public health intervention, allowing a higher cumulative infectious peak due to the low weight assigned to $J_{2,\Delta t}$.

Conversely, when the public health priority dominates the objective function ($\alpha = [0.1, 0.8, 0.1]$), a radical flattening of the epidemic curve is achieved in both examples. This epidemiological suppression is driven by a highly responsive, early, and intense escalation of the optimal vaccination control strategy $u(t)$, as captured in the bottom-right panels of Figure 5a,b. While this aggressive immunizing barrier effectively dampens the transmission mechanism, it introduces a deliberate and visible misalignment with respect to the baseline data points, clearly illustrating the competing nature of the inverse formulation. Finally, under the economic scenario ($\alpha = [0.1, 0.1, 0.8]$), the vaccination control expenditure is heavily penalized. The ALM solver dynamically suppresses prolonged or aggressive

campaigns, leading to intermediate epidemic curves that represent the most balanced and cost-effective strategy along the Pareto front. Across all regimes, the first-order Tikhonov regularization preserves the macroscopic smoothness of the piecewise linear continuous C^0 functions, completely eliminating non-physical numerical oscillations or undershoot. This simultaneous mapping fully verifies the capability of the first-discretize-then-optimize routine to isolate transparent decision-making regions for public health infrastructure.

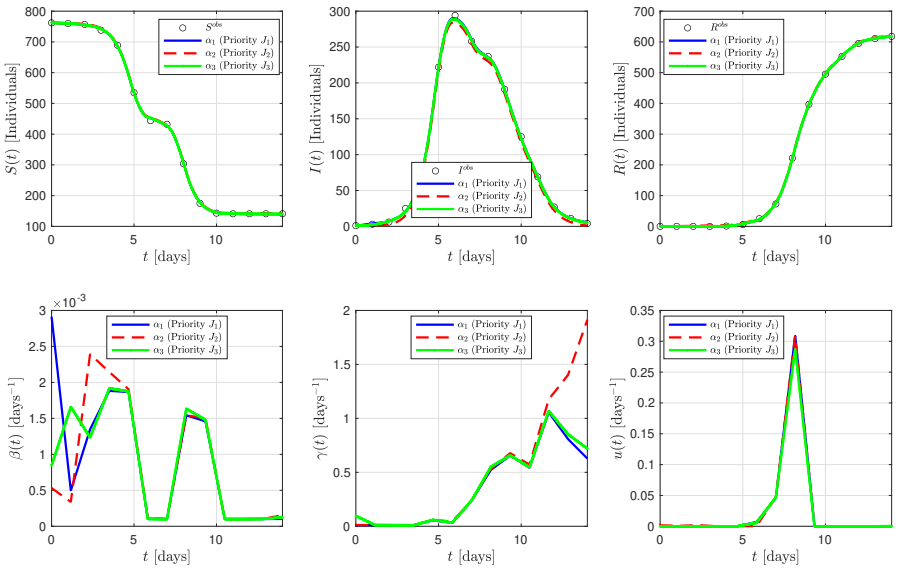

(**a**) Sensitivity analysis for Example 1 (Bilinear transmission model).

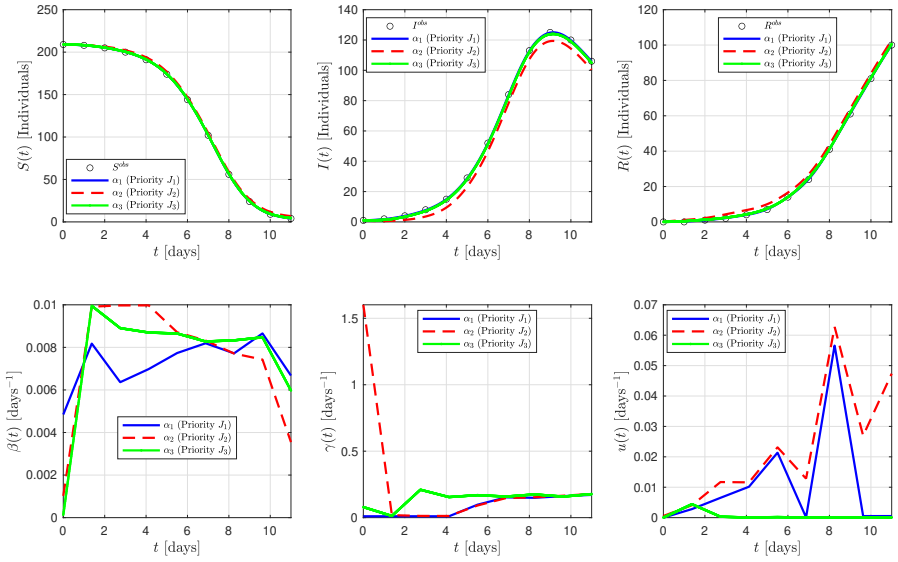

(**b**) Sensitivity analysis for Example 2 (Saturation transmission model).

Figure 5. Multi-objective results and Pareto sensitivity analysis for Examples 1 and 2. (**a**,**b**) illustrate the reconstructed optimal dynamics under different weighting profiles, comparing the simulation results and the coefficients for Examples 1 and 2, respectively.

7. Conclusions

In this paper, we have successfully developed and validated a mathematically rigorous multi-objective optimization framework for the simultaneous parameter identification and optimal vaccination control of a generalized non-linear SIR epidemic model governed by Behncke-type transmission forces. By moving beyond traditional single-objective approaches that mask critical public health conflicts behind arbitrary scalar weight choices,

this vector optimization paradigm isolates the continuous topological interactions that rule the efficient Pareto frontier. On the theoretical front, we established the global existence, uniqueness, and physical invariance of the state trajectories within the Sobolev space $W^{1,2}([0,T];\mathbb{R}^3)$ via a contraction mapping argument under the Bielecki weighted norm. Furthermore, the existence of weak Pareto-optimal strategies was proved by tracking minimizing sequences through compact Sobolev embeddings and the direct method of the calculus of variations. First-order necessary conditions were derived by leveraging the geometric Dubovitskii–Milyutin functional formalism, delivering a well-posed backward linear adjoint system and a precise vector characterization of the coupled variational inequalities. Numerically, the implementation of a robust discretization routine based on the First-Discretize-Then-Optimize paradigm allowed the successful projection of the infinite-dimensional continuous spaces onto finite-dimensional decision variables using a piecewise linear continuous C^0 functional framework. The computational architecture, resolved iteratively via an adjoint-based Augmented Lagrangian Method (ALM) coupled with the L-BFGS-B quasi-Newton algorithm, completely bypassed numerical finite-difference perturbations and proved to be highly stable, scalable, and accurate across three distinct numerical examples incorporating different saturating incidence dynamics. The reconstructed Pareto fronts provide a clear quantitative mapping of the optimal trade-offs, offering public health decision-makers a robust and verifiable tool to evaluate the intricate balance between epidemic suppression and operational expenditures.

Future research directions will focus on extending this multi-objective continuous paradigm to spatial systems governed by partial differential equations. Incorporating spatial diffusion and mobility patterns into the compartment coupling represents a major mathematical and epidemiological challenge, particularly when aligning the Pareto efficient frontier with localized georeferenced data. In this context, valuable structural insights can be drawn from recent state-of-the-art architectures, such as the spatiotemporal framework proposed for cholera dynamics with antibiotic resistance and vaccination in Zimbabwe [28]. Adapting our inverse identification algorithms and the Dubovitskii–Milyutin formalism to such complex distributed parameter environments will allow public health authorities to design targeted, proactive response mechanisms that account for both temporal progression and geographical transmission pathways.

Author Contributions: Conceptualization, A.C. and F.H.; methodology, A.C. and F.H.; software, C.I. and A.P.C.; validation, A.C., A.P.C., C.I. and F.H.; formal analysis, F.H. and A.C.; investigation, A.P.C. and C.I.; resources, A.C. and F.H.; data curation, C.I. and A.P.C.; writing—original draft preparation, A.C. and F.H.; writing—review and editing, A.C., A.P.C., C.I. and F.H.; visualization, C.I. and A.P.C.; supervision, A.C. and F.H.; project administration, F.H. and A.C.; funding acquisition, F.H. and A.C. All authors have read and agreed to the published version of the manuscript.

Funding: This research was funded by the Project supported by the Competition for Research Regular Projects, year 2023, code LPR23-03, Universidad Tecnológica Metropolitana, and the Universidad del Bío–Bío through the Regular Research Project RE2547710 and FAPEI project FP2631905.

Data Availability Statement: The original contributions presented in this study are included in the article. Further inquiries can be directed to the corresponding authors.

Conflicts of Interest: The authors declare no conflicts of interest.

References

1. Srivastav, A.K.; Ghosh, M.; Bandekar, S.R. Modeling of COVID-19 with limited public health resources: A comparative study of three most affected countries. *Eur. Phys. J. Plus* **2021**, *136*, 359. [CrossRef] [PubMed]
2. Kudryashov, N.A.; Chmykhov, M.A.; Vigdorowitsch, M. Analytical features of the SIR model and their applications to COVID-19. *Appl. Math. Model.* **2021**, *90*, 466–473. [CrossRef] [PubMed]

3. Hoang, M.T.; Ehrhardt, M. Differential equation models for infectious diseases: Mathematical modeling, qualitative analysis, numerical methods and applications. *SeMA J.* **2025**, *83*, 435–470. [CrossRef]
4. Kermack, W.O.; McKendrick, A.G. A contribution to the mathematical theory of epidemics. *Proc. R. Soc. Lond. A* **1927**, *115*, 700–721. [CrossRef]
5. Anderson, R.M.; May, R.M. *Infectious Diseases of Humans: Dynamics and Control*; Oxford University Press: Oxford, UK, 1991.
6. Martcheva, M. *An Introduction to Mathematical Epidemiology*; Springer: New York, NY, USA, 2015. [CrossRef]
7. Behncke, H. Optimal control of deterministic epidemics. *Optim. Control Appl. Methods* **2000**, *21*, 269–285. [CrossRef]
8. Coronel, A.; Huancas, F.; Isoton, C.; Tello, A. Optimal control problem and reaction identification term for carrier-borne epidemic spread with a general infection force and diffusion. *Electron. Res. Arch.* **2025**, *33*, 4435–4458. [CrossRef]
9. Fernández-Cara, E. Controllability of partial differential equations: An introduction. In *Handbook of Numerical Analysis*; Trélat, E., Zuazua, E., Eds.; Elsevier: Amsterdam, The Netherlands, 2022; pp. 165–199. [CrossRef]
10. Pareto, V. *Cours d'Economie Politique*; Rouge: Lausanne, Switzerland, 1896.
11. Ehrgott, M. *Multicriteria Optimization*, 2nd ed.; Springer: Berlin/Heidelberg, Germany, 2005. [CrossRef]
12. Jahn, J. *Vector Optimization: Theory, Applications, and Extensions*, 2nd ed.; Springer: Berlin/Heidelberg, Germany, 2010. [CrossRef]
13. Girsanov, I.V. *Lectures on Mathematical Theory of Extremum Problems*; Lecture Notes in Economics and Mathematical Systems; Springer: Berlin/Heidelberg, Germany, 1972; Volume 67. [CrossRef]
14. Kotarski, W. Characteruzation of pareto optimal points in problems with mult-eqality constraints. *Optimization* **1989**, *20*, 93–106. [CrossRef]
15. Kotarski, W. On some specification of the Dubovicki-Milutin theorem for Pareto optimal problems. *Nonlinear Anal. Theory Methods Appl.* **1990**, *14*, 287–291. [CrossRef]
16. Censor, Y. Pareto optimality in multiobjective problems. *Appl. Math. Optim.* **1977**, *4*, 41–59. [CrossRef]
17. Lobato, F.S.; Libotte, G.B.; Platt, G.M. Identification of an Epidemiological Model to Simulate the COVID-19 Epidemic Using Robust Multiobjective Optimization and Stochastic Fractal Search. *Comput. Math. Methods Med.* **2020**, *2020*, 9214159. [CrossRef] [PubMed]
18. Libotte, G.B.; Lobato, F.S.; Platt, G.M.; Neto, A.J.S. Determination of an optimal control strategy for vaccine administration in COVID-19 pandemic treatment. *Comput. Methods Programs Biomed.* **2020**, *196*, 105664. [CrossRef] [PubMed]
19. Lobato, F.S.; Steffen, V., Jr. A new multi-objective optimization algorithm based on differential evolution and neighborhood exploring evolution strategy. *J. Artif. Intell. Soft Comput. Res.* **2011**, *1*, 259–267.
20. Lobato, F.S.; Machado, V.S.; Steffen, V., Jr. Determination of an optimal control strategy for drug administration in tumor treatment using multi-objective optimization differential evolution. *Comput. Methods Programs Biomed.* **2016**, *131*, 51–61. [CrossRef] [PubMed]
21. Adams, R.A. *Sobolev Spaces, Pure and Applied Mathematics*; Academic Press: New York, NY, USA, 1975; Volume 65.
22. Evans, L.C. *Partial Differential Equations*; American Mathematical Society: Providence, RI, USA, 1997.
23. Coddington, E.A.; Levinson, N. *Theory of Ordinary Differential Equations*; McGraw-Hill: New York, NY, USA, 1955.
24. Jahn, J. *Introduction to the Theory of Nonlinear Optimization*, 4th ed.; Springer: Cham, Switzerland, 2020. [CrossRef]
25. Anonymous. Influenza in a boarding school. *Br. Med. J.* **1978**, *1*, 587.
26. Bolker, B. *EEID Lecture Notes: Trajectory Matching and Fitting Epidemic Models to Data*; McMaster University: Hamilton, ON, Canada, 2011.
27. Chowell, G.; Echevarría-Zuno, S.; Viboud, C.; Simonsen, L.; Tamerius, J.; Miller, M.A.; Borja-Aburto, V.H. Characterizing the epidemiology of the 2009 influenza A/H1N1 pandemic in Mexico. *PLoS Med.* **2011**, *8*, e1000436. [CrossRef] [PubMed]
28. Wu, P.; Zhang, S.; Wang, X.; Wang, H. Spatiotemporal cholera dynamics with antibiotic resistance and vaccination via demographic-epidemic data in Zimbabwe. *J. Math. Biol.* **2026**, *92*, 42. [CrossRef] [PubMed]

Disclaimer/Publisher's Note: The statements, opinions and data contained in all publications are solely those of the individual author(s) and contributor(s) and not of MDPI and/or the editor(s). MDPI and/or the editor(s) disclaim responsibility for any injury to people or property resulting from any ideas, methods, instructions or products referred to in the content.